JOURNAL OF GEOPHYSICAL RESEARCH, VOL. 103, NO. B2, PAGES 2673–2692, FEBRUARY 10, 1998

Global mapping of topography on transition zone velocity discontinuities by stacking *SS* precursors

Megan P. Flanagan and Peter M. Shearer

Cecil H. and Ida M. Green Institute of Geophysics and Planetary Physics, Scripps Institution of Oceanography
University of California at San Diego, La Jolla

Abstract. We stack long-period, transverse-component seismograms recorded by the Global Digital Seismograph Network (GDSN) (1976-1996), Incorporated Research Institutions for Seismology-International Deployment of Accelerometers (IRIS-IDA) (1988-1996), and Geoscope (1988-1996) networks to map large-scale topography on the 410- and 660-km seismic velocity discontinuities. Underside reflections from these discontinuities arrive as precursors to the *SS* phase, and their timing can be used to obtain global variations of the depth to the reflectors. We analyze over 13,000 records from events m_b >5.5, focal depth < 75 km, and range 110° to 180° by picking and aligning on *SS*, then stacking the records along the theoretical travel time curves for the discontinuity reflections. Separate stacks are obtained for 416 equally spaced caps of 10° radius; clear 410- and 660-km reflections are visible for almost all of the caps while 520-km reflections are seen in about half of the caps. The differential travel times between the precursors and the *SS* arrival are measured on each stack, with uncertainty estimates obtained using a bootstrap resampling method. We then compute discontinuity depths relative to the isotropic Preliminary Reference Earth Model (PREM) at 40-s period, correcting for surface topography and crustal thickness variations using the CRUST5.0 model of *Mooney et al.* [1995], and for upper mantle *S* velocity heterogeneity using model S16B30 of *Masters et al.* [1996]. The resulting maps of discontinuity topography have more complete coverage than previous studies; observed depths are highly correlated between adjacent caps and appear dominated by large-scale topography variations. The 660-km discontinuity exhibits peak-to-peak topography of about 38 km, with regional depressions that correlate with areas of current and past subduction around the Pacific Ocean. Large-scale topography on the 410-km discontinuity is lower in amplitude and largely uncorrelated with the topography on the 660-km interface. The width of the transition zone, W_{TZ}, as measured by the separation between the 410- and 660-km discontinuities, appears thickest in areas of active subduction (e.g., Kurils, Philippines, and Tonga) and thins beneath Antarctica and much of the central Pacific Ocean. Spatial variations in W_{TZ} appear unrelated to ocean-continent differences but do roughly correlate with the S16B30 velocities in the transition zone, consistent with a common thermal origin for both patterns. The lower-amplitude 520-km reflector is more difficult to resolve but appears to be a global feature as it is observed preferentially for those bounce point caps with the most data.

1. Introduction

Mapping global topography on the transition zone velocity discontinuities has long been an important objective in global geophysics as these boundaries are expected to have undulations associated with thermal, chemical, and dynamic processes in the Earth's interior. The mantle transition zone is an anomalous region between about 400 and 750 km depth in the Earth in which density and seismic velocities increase much more steeply than in the surrounding mantle, with particularly sharp changes noted near depths of 410, 520, and 660 km. A complete understanding of the dynamics of mantle convection, plate-scale flow, and the distribution of geochemical reservoirs in the Earth is strongly dependent upon our ability to characterize the composition, structure, and physical properties of the transition zone [e.g., *Bina*, 1991].

Paper number 97JB03212.
0148-0227/98/97JB-03212$09.00

Results of laboratory experiments at high pressures and temperatures suggest that the velocity and density increases within the transition region correlate with pressure-induced phase transformations in olivine $(Mg,Fe)_2SiO_4$, the major mineralogical component of the upper mantle [e.g., *Ringwood*, 1975; *Jackson*, 1983; *Ito and Takahashi*, 1989]. These phase transitions include the collapse of α olivine to β (modified spinel) structure near 410 km, β to γ-spinel near 520 km, and the dissociation of γ-spinel to silicate perovskite $(Mg,Fe)SiO_3$ and magnesiowüstite (Fe,Mg)O near 660 km depth. While this interpretation is widely invoked, it has also been challenged by models of mantle composition and dynamics which argue that small compositional changes may also be present close to or coincident with the depths of these phase changes [e.g., *Anderson and Bass*, 1986; *Duffy and Anderson*, 1989]. In particular, it has been proposed that the 660-km discontinuity may represent a change in chemical composition, and although its interpretation as a phase boundary is now rather universally established, recent work [*Jeanloz*, 1991; *Ita and Stixrude*, 1992; *Stixrude et al.*, 1992; *Bina and Kumazawa*, 1993] has indicated that a change in bulk

chemistry (enrichment in Fe or Si or both) may be necessary in addition to a phase transition in order to simultaneously satisfy the observed density and seismic velocity jumps. Resolving the nature of the transition zone discontinuities is crucial for evaluating the diversity of structural and dynamic models as the continuing debate over mantle stratification and convection still centers on these major phase transitions and how they may affect the pattern of flow [*Anderson and Bass*, 1986; *Creager and Jordan*, 1986; *Ringwood and Irfune*, 1988; *Silver et al.*, 1988]. Detailed seismic observations of the transition zone may help address this issue, as well as better constrain the bulk mantle composition through comparisons with geochemistry and high-pressure mineral physics experiments.

In addition, the major transition zone discontinuities near 410- and 660-km depth (hereafter referred to as the 410 and 660, although their actual depths may vary) are expected to have a significant effect on mantle convection. The negative Clapeyron slope (the gradient of the phase boundary in pressure/temperature space) for the olivine phase change at 660 km implies that this boundary will move downward in response to colder temperatures. This introduces lateral density perturbations at the interface that will act to inhibit thermally driven flow across the boundary; thus the magnitude of the observed topography on the 660-km discontinuity is an important constraint in modeling mantle convection [e.g., *Phipps Morgan and Shearer*, 1993]. By using laboratory measurements of the P-T curve for the 410 and 660 phase boundaries, discontinuity depths can be used to infer in situ mantle temperatures, and the amplitude of discontinuity topography provides a measure of the size of lateral temperature variations in the transition zone.

Previous studies by *Shearer* [1991, 1993] and *Shearer and Masters* [1992] used *SS* precursor observations to demonstrate that large-scale variations in the depths to the 410 and 660 exist and are resolvable with long-period data. We continue this work here but apply improved analysis methods on a significantly larger data set (made possible by the ongoing expansion of the global seismic networks) to produce detailed maps of discontinuity topography with more complete spatial coverage. In addition, we expand our efforts to include the often elusive 520-km discontinuity and identify some spatial variations in its depth. Finally, we compare our results to recent tomographic images of upper mantle velocity structure and other recent seismological and mineral physics studies of transition zone discontinuities.

2. SS Precursor Data Set

Our approach to mapping transition zone discontinuity topography involves observations of *SS* precursors, the geometry of which are shown in Figure 1 for epicentral distances of 120°, 140°, and 160°. Underside reflections off the 410- and 660-km velocity discontinuities are recorded as precursors to the surface reflected *SS* phase; they arrive ahead of *SS* and the difference in time between the waves can be used to constrain the depths of the discontinuities. The use of differential times is more robust than measuring absolute travel times, as the similarity of ray paths between the surface reflection (*SS*) and the precursors (termed *SdS*, where *d* is the discontinuity depth) minimizes the effect of source and receiver structure; the differential time is mainly sensitive to the vicinity of the *SS* bounce point.

We use long-period waveforms from earthquakes of focal depth < 75 km, in the epicentral distance range 110° to 180°, and having a body wave magnitude $m_b > 5.5$. The data are collected from the Global Digital Seismograph Network (GDSN) (1976-1996), Incorporated Research Institutions for Seismology-International Deployment of Accelerometers (IRIS-IDA) (1988-1996), and Geoscope (1988-1996) digital

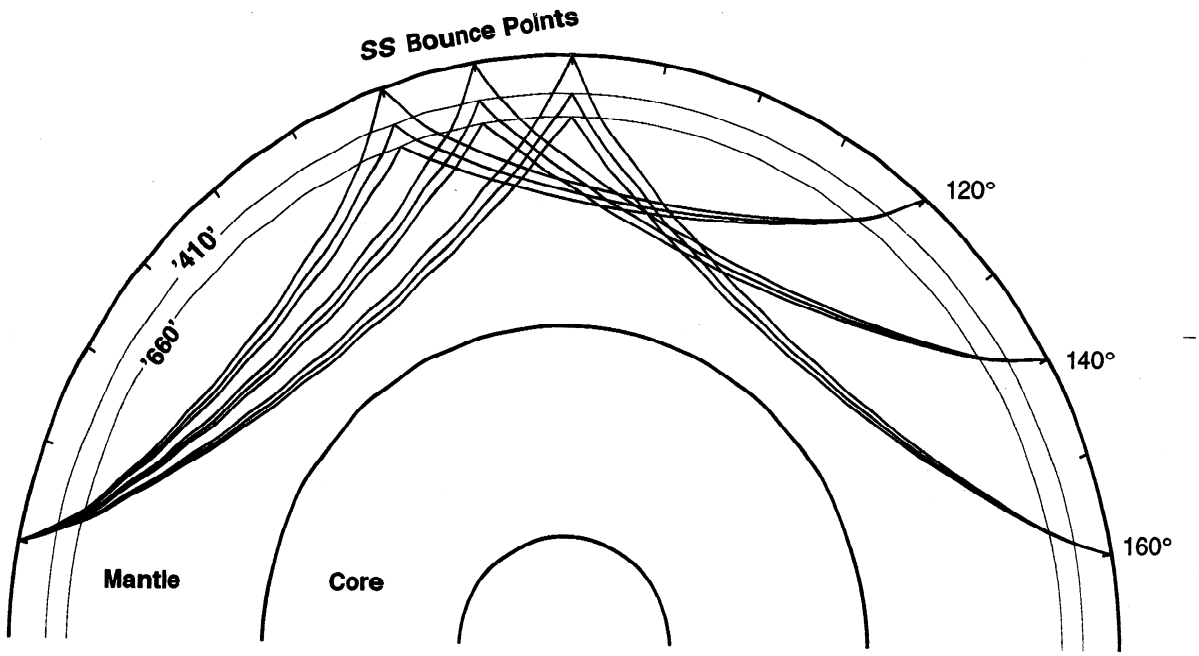

Figure 1. Geometry of the surface-reflected *SS* and underside reflections *S*410*S* and *S*660*S* (i.e., *SdS*, where *d* is the discontinuity depth) phases for source-receiver distances of 120°, 140°, and 160°; ray paths are computed using the iasp91 velocity model [*Kennett*, 1991]. Structure near the source and receiver has little effect on *SS-SdS* differential times, as the ray paths are very similar except near the bounce point locations.

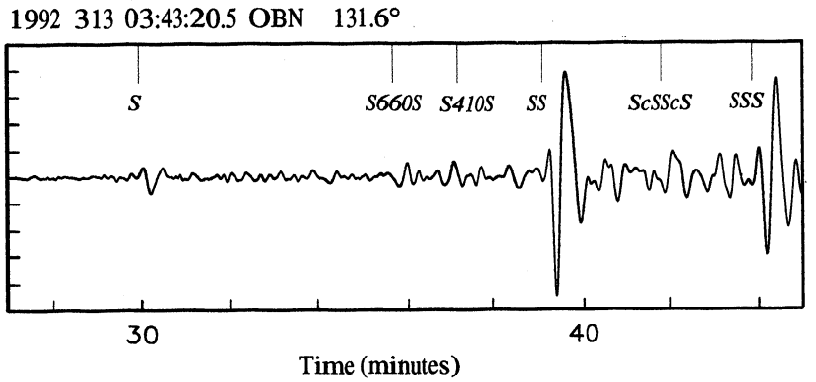

Figure 2. Transverse-component seismogram from an m_b = 6.1 event in the Tonga subduction zone recorded on the long-period channel at station OBN at a range of 131.6°. The theoretical arrival times of *SS* and the precursors *S660S* and *S410S* are indicated at the top.

networks. The range of focal depths is selected to minimize interference from the depth phase *sSS*, and the magnitude criterion ensures good excitation of teleseismic energy. The distance range 110° to 180° is chosen to avoid interference with the topside multiples at close ranges (see the *Ss*410s and *Ss*660s travel time curves in Plate 1). As we maintain a growing, on-line database of 1 Hz sample-rate data, some preprocessing of the data is done to establish uniformity. All records are filtered to the GDSN long-period instrument response (at station ANMO, January 1, 1985). We use only the transverse component, obtained by rotating the horizontal components using the epicentral information provided in the monthly Preliminary Determination of Epicenters (PDE) bulletins of the U.S. Geological Survey.

We begin our analysis by computing a local measure of the signal-to-noise ratio of *SS* obtained from the maximum amplitudes in windows extending ±60 s from the theoretical *SS* arrival time calculated using the iasp91 velocity model [*Kennett*, 1991]. Using a signal-to-noise cutoff of three in this automatic editing procedure results in a total of about 25,000 seismograms from 5110 earthquakes recorded at 223 stations. Next, we visually inspect each seismogram, rejecting those with poor quality arrivals, and pick the first major swing of the *SS* pulse. This reduces the number of data to 13,469 seismograms, graded with an A, B, or C based on the signal-to-noise ratio and the simplicity and clarity of the *SS* reference phase. Figure 2 is an example seismogram from an earthquake in the Tonga subduction zone, recorded at station OBN in Russia at 132° range. In this example, energy arrives at the predicted time for the underside reflections off the transition zone velocity discontinuities, but this is rarely observed on individual records since the discontinuity reflections are normally less than 5% of the amplitude of the main *SS* pulse. More commonly, dozens of records must be stacked to obtain clear discontinuity reflections.

An advantage of *SS* precursors, compared to other mantle discontinuity phases, is the comprehensive global coverage they provide. Figure 3 shows a map of the *SS* surface reflection points of the 11,207 quality A and B records used in this study. This approximately doubles the dataset used by *Shearer* [1993] and fills in many of the gaps in the older models. Note the excellent distribution of bounce points in

Figure 3. Global distribution of the *SS* bounce points of the 11,207 seismograms used in this study to map discontinuity topography. Note the extensive coverage in the northwest and central Pacific Ocean and the Indian Ocean, while sparse data are seen in South America, Australia, and parts of Africa. Plate boundaries are shown by the dashed lines.

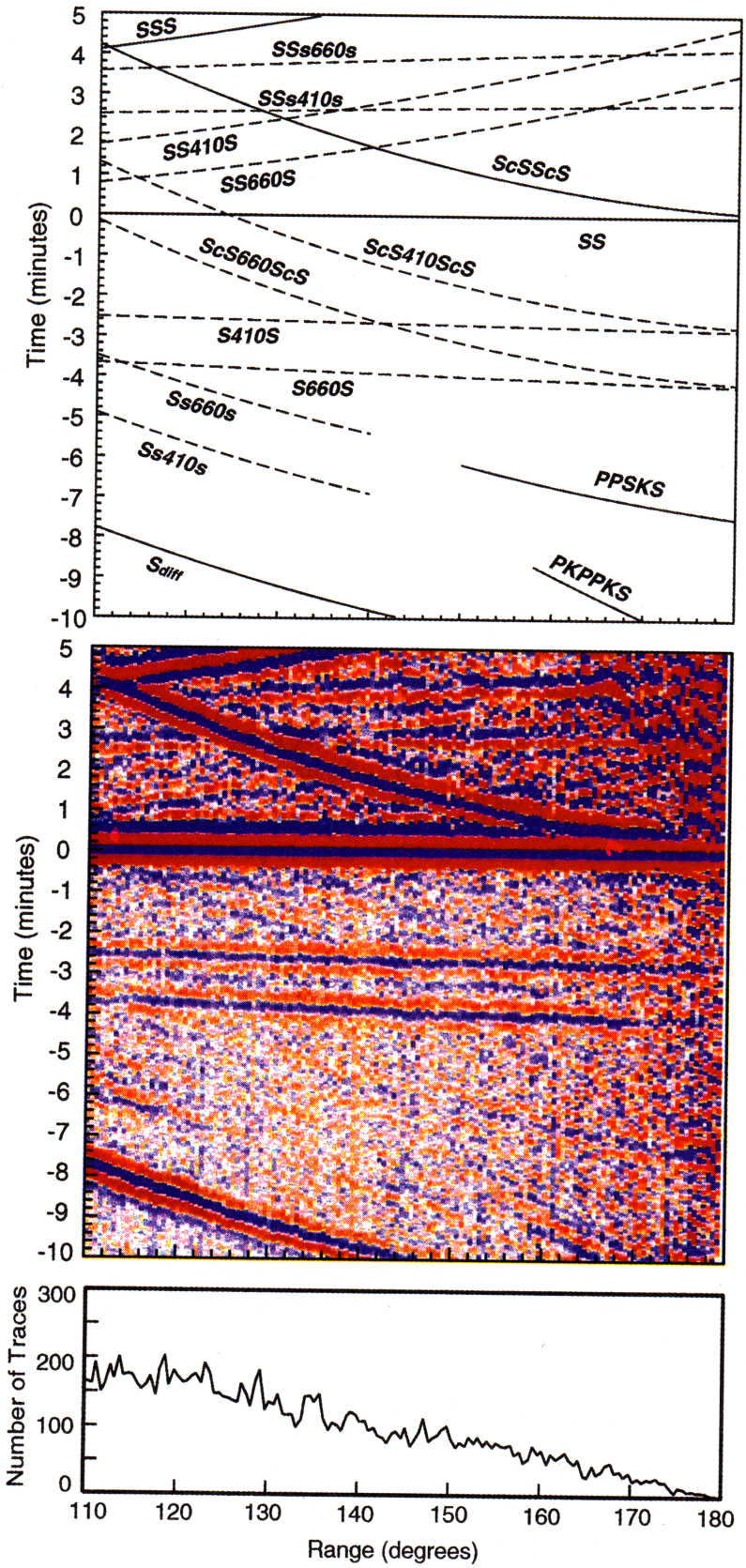

Plate 1. Stacked time versus range image showing *SS* and its precursors. This record section comprises 13,469 traces stacked in 0.5° range bins, the distribution of which are shown in the histogram below. *SS* is shifted to zero time and normalized to unit amplitude. Positive amplitudes are blue and negative amplitudes are red, with the scale ranging from ± 6% of the *SS* peak amplitude. The primary arrivals S_{diff}, *SS*, and *ScSScS* are saturated at this scale, but the underside reflections *S*410*S* and *S*660*S* are clearly seen at 190 s and 230 s prior to *SS*. The top plot contains the travel-time curves computed from iasp91 (for 0 km focal depth) for the primary phases (solid lines) and transition zone discontinuity phases (dashed) in this time window.

the northwest and central Pacific Ocean as well as the Indian Ocean and the good coverage in the western United States and Canada, north Atlantic Ocean, Antarctica, and eastern Asia. However, some areas remain only marginally covered, including South America, Australia, and Africa. The inclusion of data from recently installed stations of both the Geoscope and GDSN networks in the southern hemisphere has provided the greatest improvement in *SS* bounce point coverage.

3. Stacking Procedure

We stack the seismograms in two ways: (1) we combine all of the data to produce a single time versus range image of the *SS* precursor wave field that shows the discontinuity phases, and (2) we divide the data by bounce point location and stack along the travel time curves of the precursors to obtain reflection profiles of the upper mantle which can be used to constrain discontinuity depths in localized regions. Our current efforts to image global topography on the transition zone velocity discontinuities are similar to previous work by *Shearer and Masters* [1992] and *Shearer* [1993], but we now analyze a significantly larger data set and have implemented the following improvements to our methodology: (1) we manually edit and align the *SS* pulses rather than relying on an automatic algorithm, (2) we weight each seismogram in the stack by its signal-to-noise ratio to give greater emphasis to the higher-quality data, (3) we apply a mild low-pass filter and deconvolve each trace by the *SS* reference pulse prior to stacking, (4) we explicitly account for the geographically nonuniform distribution of data within individual bounce point caps, and (5) we apply corrections for upper mantle heterogeneity using a new crustal model and an improved *S* wave velocity model.

To produce the global stacks, all records are aligned on the *SS* pick time and stacked on the *SS* phase; negative polarity records are reversed prior to stacking. The records in each bin are individually weighted by a measure of the signal-to-noise in a window 300 to 100 s prior to *SS*, and the entire record is normalized to the maximum amplitude in this window. Plate 1 is a time versus range plot comprising all 13,469 records (A, B, and C quality) stacked in 0.5° bins over the distance interval 110° to 180°. Blue and red indicate positive and negative amplitudes, respectively; *SS* is normalized to unit amplitude and the scale is ± 6%. The *SS* reference pulse is the bright blue streak aligned at zero time. Note the primary phases S_{diff}, *SS*, *SSS*, *ScSScS* saturate at this scale, but several secondary arrivals are evident. The precursors *S*410*S* and *S*660*S* (the two blue streaks) are clearly seen as coherent energy preceding *SS* by about 160 s and 230 s over the entire distance range. A weaker arrival at about 190 s results from a reflector near 520 km depth; as discussed by *Shearer* [1996], this cannot be explained as a sidelobe artifact from the *S*410*S* and *S*660*S* phases. Note that the stack becomes more noisy, for example, at distances of 170° to 180°, where there are fewer seismograms within each range bin, as shown by the histogram at the bottom. Plotted at the top are the theoretical travel time curves calculated from iasp91 [*Kennett*, 1991]. In addition to the *SdS* reflections that are the focus of this paper, a variety of topside and bottomside reflections and conversions from the transition zone discontinuities can also be seen in this stack, some over the entire distance range: *SS*s410s, *SS*s660s, *SS*660S, and *ScS*660*ScS*; some over limited epicentral ranges: *Ss*410s and *Ss*660s. Leakage from *P/SV* polarized phases onto the transverse component is sometimes seen; this explains the apparent *PPSKS* and *PKPPKS* arrivals at ranges greater than 155°.

To explore lateral variations in discontinuity depths, we produce waveform stacks by binning the data according to their bounce point location and then collapsing the energy along an *SdS* travel time curve to produce reflectivity profiles as a function of time. In this way we combine seismograms with different epicentral ranges but with similar bounce point location. We apply a cap-averaging scheme that uses 416 circular caps of 10° radius that are spaced approximately 10° apart. This cap spacing is comparable in size to the *SdS* Fresnel zones [*Shearer*, 1993], but there is some sharing of data between adjacent caps resulting in an additional smoothing of the data.

We apply this cap-averaging procedure to only the 11,207 A and B quality waveforms. As in the composite image, each trace is weighted by a measure of the signal-to-noise ratio of the *SS* pulse prior to stacking. Each record is then normalized by deconvolution and filtering to reduce noise and sidelobe artifacts. The *SS* pulse is deconvolved from the entire seismogram in order to account for differences in the shape of the reference pulse (which are mostly a result of source depth variations). This is done by windowing the *SS* pulse and dividing the entire seismogram by the reference wavelet in the frequency domain. An acausal, low-pass filter is used to stabilize the deconvolution and reduce high-frequency noise. This filter produces symmetric pulse shapes with minimal sidelobes, as seen in Figure 4 of the waveform stacks. After several trial runs to check the stability of the deconvolution by varying both the length of the wavelet and the frequency band over which the deconvolution is performed, we choose a window of -30 s before and 50 s after the peak amplitude time of *SS* and a low-pass filter to 0.06 Hz with a corner at 0.03 Hz. The deconvolution improves the resolution of closely spaced peaks on the seismogram and is particularly useful in resolving the 520 peak. In performing the deconvolution, we implicitly assume that the *SdS* pulse shapes are identical to the *SS* pulse. This is only approximately true, as *SS* travels two additional legs through the crust and upper mantle compared to *SdS*. The waveform differences are probably fairly minor for oceanic *SS* bounce points [see *Shearer*, 1996] but could be significant in areas of thick continental crust. This effect is not likely to significantly bias 410 and 660 depth estimates but could have some influence on 520 observations in these regions.

After deconvolution and filtering, we separately stack the *SS* reference pulse and the precursor wave field for all seismograms within each cap. The precursors are stacked along the predicted travel time curve for *S*550*S* (i.e., intermediate between the *S*410*S* and *S*660*S* travel time curves) to produce reflectivity profiles of the upper mantle. As examples, six of these summation traces are shown in Figure 4 which illustrates a variety of different cap locations, each containing a different number of seismograms. The thick trace is the actual waveform stack, and the thin lines are 95% confidence limits computed using a bootstrap method [e.g., *Efron and Tibshirani*, 1991] which randomly resamples (200 times) the data in each cap prior to stacking. Note that these limits grow larger as the number of records decreases and the signal-to-noise ratio decreases. The reference *SS* phase, aligned at zero time and normalized to unit amplitude, is shown to the right of the dashed vertical line. The left portion

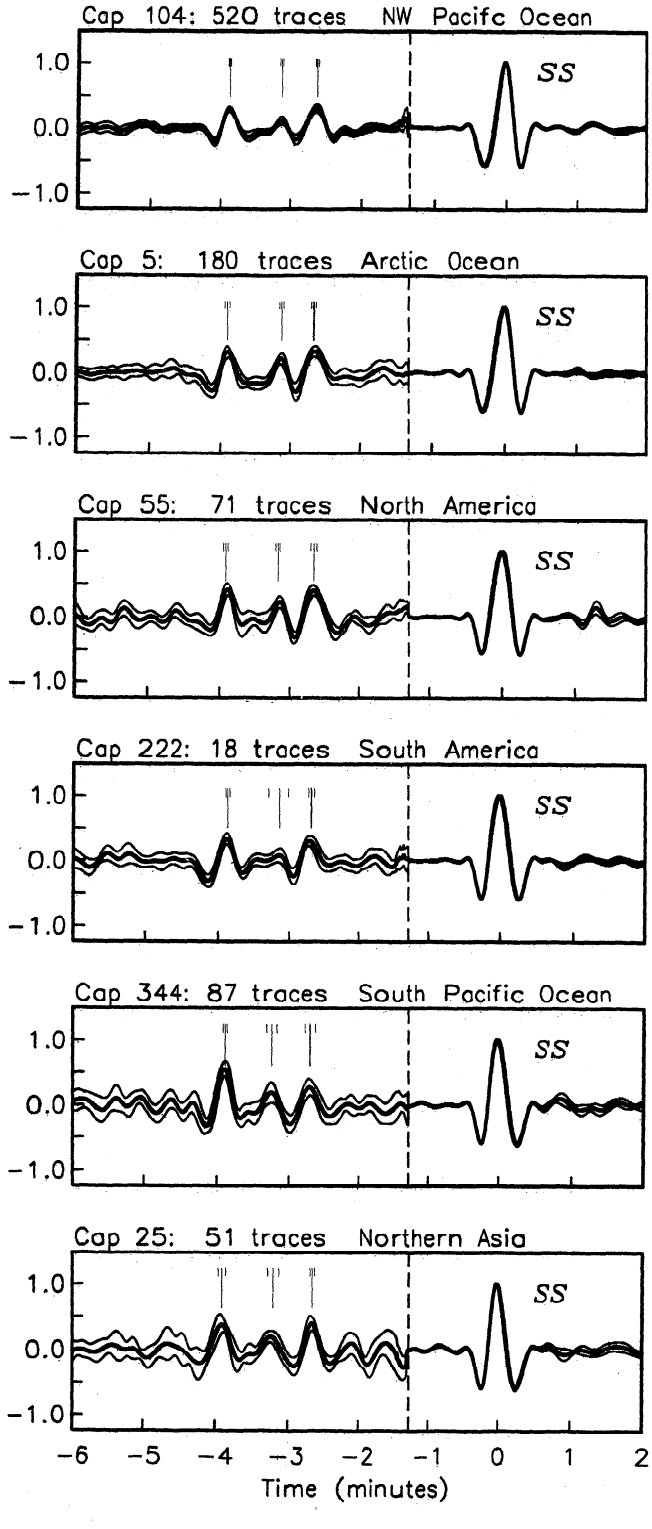

Figure 4. Waveform stacks, after deconvolution and filtering, of six caps representing different geographic regions and numbers of traces. The thick trace is the actual stack, and the thin lines represent 95% confidence limits calculated using a bootstrap resampling algorithm. Note the precursor amplitudes to the left of the vertical dashed line are amplified by a factor of 10. The 660, 520, and 410 peaks are seen from left to right, with the small vertical lines indicating their individual time estimates and standard errors. These are computed by measuring the *SS-SdS* differential travel times, then converting the times to depths assuming a reference radial velocity model (PREM at 40 s).

of the plot is the result of stacking the precursor wave field along the predicted travel time curve for *S550S* to a reference range of 138°. The *S550S* travel time curve is approximately parallel to both *S410S* and *S660S* and adjusts for the bulk of the slowness differences between the precursors and *SS*; the slight additional timing shifts between this curve and the precursors have a negligible effect on the stacked waveforms at long periods [see *Shearer*, 1996]. The amplitude of the precursor stack is exaggerated by a factor of 10 for display purposes. Peaks from the 410-, 520-, and 660-km reflectors can be seen in all of these examples, although the 520-km peak is marginal in the South American stack which contains only 18 seismograms.

Next, we measure the time of the precursor peaks on the waveform stack for each of the 416 caps with an automated procedure that uses the bootstrap resampling technique to obtain error estimates. These peak times, together with their standard errors, are marked for the six examples in Figure 4. Note that the peaks appear at slightly different times for these subsets of the data, indicating the presence of discontinuity topography and/or lateral velocity variations in the crust and upper mantle. Occasionally, this method will return times for peaks that are not well resolved in the waveform stacks. Thus we visually inspect the reflectivity profiles and discard those caps with erroneous or ambiguous results which are commonly due to the presence of multiple peaks or simply very low signal-to-noise ratios. After this editing, we obtain 340 times for *S410S*, 199 times for *S520S*, and 342 times for *S660S*. The smaller number of times obtained for *S520S* reflects the generally weaker amplitude of this phase and does not necessarily indicate that the 520-km reflector is not a global feature (discussed below). In addition, we obtain estimates for the differential time between *S410S* and *S660S* that are used to constrain the thickness W_{TZ} of the layer between the 410 and 660 reflectors (for convenience, we term W_{TZ} the width of the transition zone, although often the transition zone is considered to extend somewhat below the 660-km interface). In this case, we obtain estimates from 306 caps in which both the *S410S* and *S660S* peaks can be clearly seen. Some of the stacks hint at the presence of additional discontinuities at depths above 410 km or below 660 km, but these are typically close to the noise levels and are not a subject of this paper.

4. Obtaining Accurate Discontinuity Depths

To convert *SS-SdS* differential times to discontinuity depths, a reference velocity model is required. We begin by using the isotropic version of the Preliminary Reference Earth Model (PREM) at 40 s period [*Dziewonski and Anderson*, 1981] and trace rays through this model to obtain travel time curves for *SS* and *SdS* at a range of depths. For simplicity in this calculation, we do not adjust the PREM discontinuity depths at 400 and 670 km but simply assume hypothetical reflectors at other depths. At our stacking reference range of 138°, it is then a simple matter to interpolate between these curves to convert *SS-SdS* differential times to discontinuity depths. In a similar way, the standard errors of the precursor peak times are translated into limits on the depth estimates. In Figure 5 we plot the apparent discontinuity depths for the 410, 520, 660, and the transition zone thickness (W_{TZ}) as perturbations about their global mean values. Crosses indicate deeper regions, and diamonds indicate shallower regions with the size of the symbol scaling with the amplitude

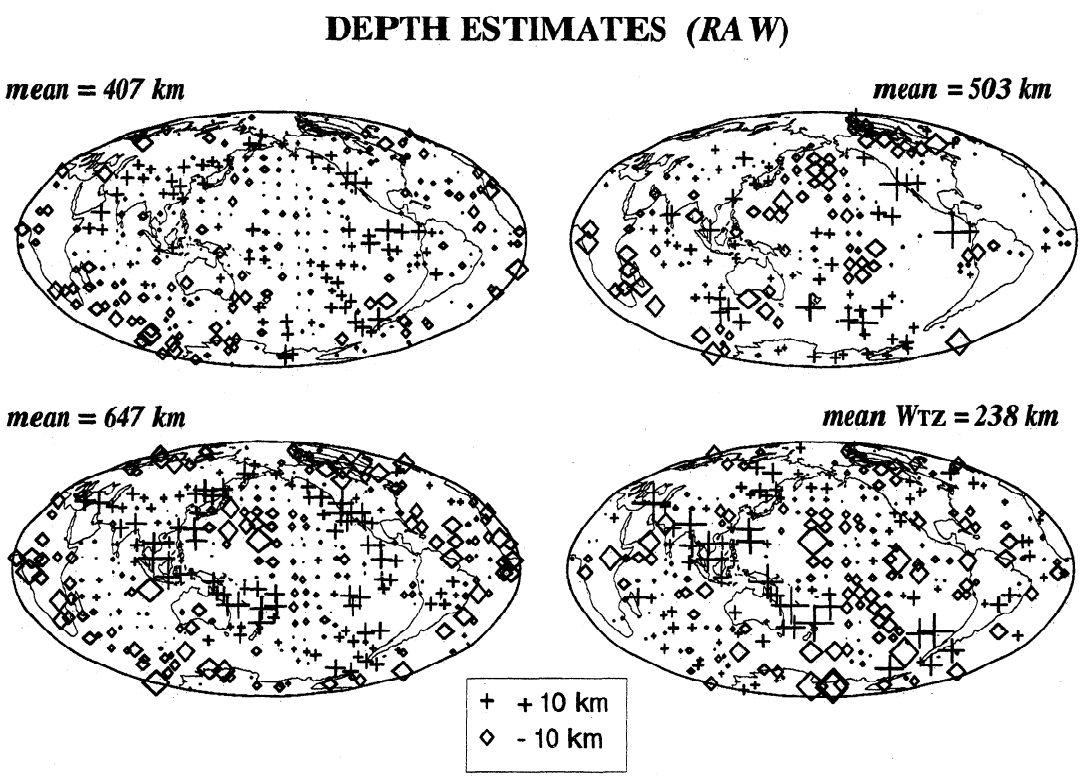

Figure 5. Map of depth estimates for the 410, 520, 660, and transition zone thickness (W_{TZ}), plotted at the centroid location of bounce points for each cap. Crosses indicate depressions and diamonds indicate elevations relative to the mean discontinuity depth, or thickness, as indicated. Depth estimates are plotted only if the cap contains 10 or more seismograms and the standard error is less than 10 km for the 410 and 660 and less than 15 km for the 520 and W_{TZ}.

of the topography. Depth estimates are plotted only if the cap contains 10 or more seismograms and has a standard error in depth of less than 10 km for the 410 and 660 reflectors or less than 15 km for the 520 and W_{TZ}. The symbols are not plotted at the center of each cap; instead they are shown at the mean location of the *SS* bounce points that are included in the cap. Because of this, the plotted symbols are not evenly spaced at the nominal 10° spacing of the caps, but they more accurately reflect the true distribution of the data in the case where the data coverage within the cap is unevenly distributed or clustered near the edge of the cap. These maps show peak to peak topography of roughly 40 km for the 410 (388-430 km) and about 50 to 60 km for the 520 (478-535 km), the 660 (623-673 km), and the W_{TZ} (212-276 km), with large-scale coherent patterns of elevated and depressed regions. Some agreement in discontinuity depths between neighboring caps should be expected due to the partial overlap of data between adjacent caps, but the average correlation length of the topography is significantly greater than the cap separation.

However, these depth estimates are likely to be biased because we have thus far neglected the effect of lateral variations in surface topography, crustal structure, and upper mantle shear wave velocities. These will change the observed *SS-SdS* times by altering the two-way travel time of *S* waves between the discontinuities and the surface. Thus the patterns shown in Figure 5 may not represent real differences in discontinuity depths but simply reflect velocity differences in the overlying mantle. In addition, there are likely to be errors in the mean discontinuity depths if the adjustment of PREM to the crustal model produces a baseline shift in travel times through the crust and uppermost mantle. Obtaining reliable corrections for these effects is important, as the size of these corrections is comparable to the topographic signals that we observe and mantle temperature estimates based on laboratory pressure-temperature results for the appropriate mineral phase changes will depend upon the accuracy of the absolute discontinuity depths.

We begin by correcting the *SS* travel times for the effect of topography and crustal structure at the *SS* surface bounce points, using the recent regionalized global crustal model CRUST5.0 [*Mooney et al.*, 1995]. This model provides surface topography and bathymetry (taken from the ETOPO5 database of the National Geophysical Data Center, 1988) as well as crustal thicknesses and velocities within 5° by 5° blocks. We smooth these corrections to a resolution closer to the Fresnel zone of our observations by averaging the crustal thickness corrections within circles of 18° diameter, centered on the mean *SS* bounce point location within each cap. This avoids generating artificially sharp changes in the discontinuity depths as the *SS* bounce points cross an ocean-continent margin where the crustal thickness changes abruptly. The computed corrections to the *SS* times at the 138° reference range are plotted at the top of Figure 6. Note that the *SS* times predicted are earlier for oceanic bounce points compared to continental bounce points due to the thicker crust and higher topography on the continents. Within the continents, the *SS* times are most delayed in regions of thickest crust, such as the Tibetan plateau and the

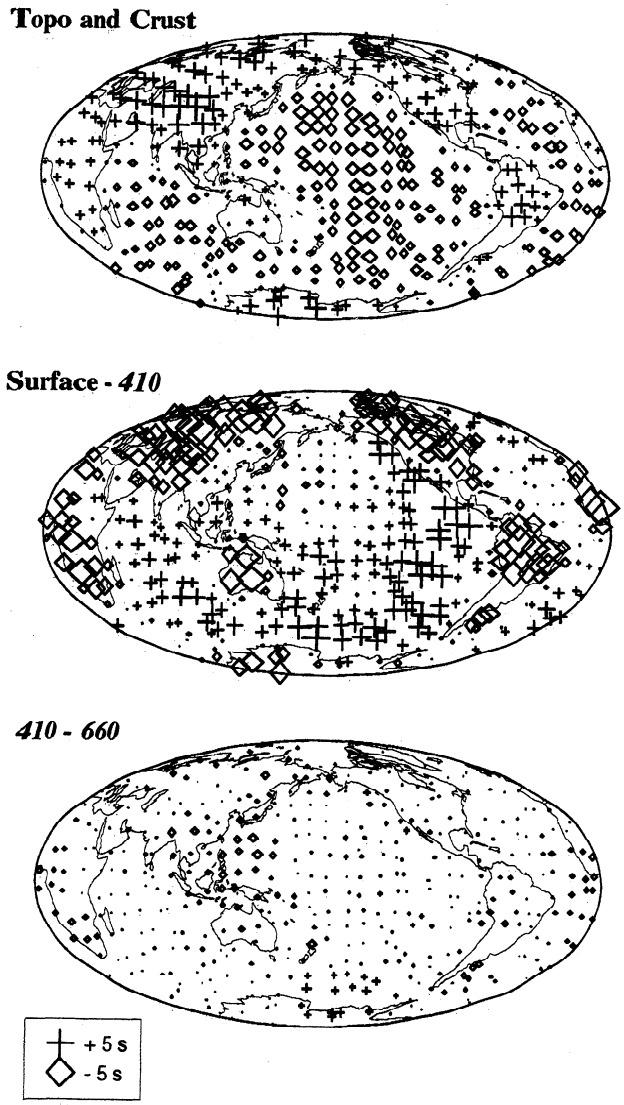

Figure 6. Crust, topography, and upper mantle corrections to *SS* travel times computed for the average source-receiver range of the data in each cap and plotted at the centroid cap locations as in figure 5. (top) Surface topography and crustal thickness differences computed from CRUST5.0 [*Mooney et al.*, 1995]; note the delays on the continents (crosses) relative to the oceans (diamonds). Shear velocity model S16B30 [*Masters et al.*, 1996] structure for (middle) the upper mantle and (bottom) transition zone; the time corrections above 410 km are much larger than between 410 and 660 km.

Andes. The crustal corrections range from -3.1 to 4.2 s relative to a mean value of -0.07 s.

Next, we compute corrections for lateral *S* velocity variations in the upper mantle using the tomographic model S16B30 [*Masters et al.*, 1996]. This model is derived from normal modes, surface wave dispersion measurements and body wave travel times and is parameterized laterally by spherical harmonics up to degree 16 and radially by 30 natural cubic B splines. S16B30 assumes the crustal structure of CRUST5.0, so use of this model to adjust our *SS*-*SdS* times is consistent with the corrections discussed above. Because the lateral velocity gradients in S16B30 are relatively smooth, we compute our corrections as the integrated travel time perturbation between the surface and each discontinuity, using the average bounce point locations and the ray parameter for *SS* at 138° without regard to individual ray azimuths or small differences between the *SS* and *SdS* ray paths at depths below the discontinuities (see Figure 1). The errors introduced by this approximation are almost certainly much smaller than those introduced by the uncertainties in the velocity model itself.

Figure 6 (middle) shows the calculated corrections to the *S*410*S* times; these range from -6.4 to 5.0 s relative to an average value of 0.03 s. The velocity heterogeneity in S16B30 is concentrated at shallow depths; thus the pattern seen in the *S*660*S* corrections is very similar to the *S*410*S* results. Differences in the predicted times of *S*410*S* and *S*660*S* (Figure 6, bottom), sensitive to the velocity anomalies within the transition zone, are relatively small. The 410-660 corrections are -1.4 to 1.7 s relative to an average of 0.01 s. To some extent, the corrections for three-dimensional velocity structure trade-off with those for crustal structure; the crustal corrections show time delays on continents relative to oceans, and conversely, the velocity corrections show fast arrivals under the continents and delays under the oceans.

The size of the crustal and mantle corrections is significant in terms of discontinuity topography. For example, a 5-s difference in the *SS* time translates to a 12- to 15-km change in the inferred upper mantle discontinuity depths. The CRUST5.0 and S16B30 models represent a major improvement over the older models used to correct discontinuity topography by *Shearer* [1993]. However, it is likely that some errors remain, and these will introduce some bias into our results. These biases can be reduced by focusing on W_{TZ}, the transition zone width, because errors in the corrections at shallow depths (where the velocity heterogeneity is strongest) will affect the 410 and 660 depth estimates by comparable amounts.

The presence of discontinuity topography will have some influence on tomographic models of upper mantle shear velocity which compute perturbations to reference one-dimensional Earth models assuming uniform discontinuity depths. For example, a depression in the 660-km discontinuity will increase the volume of the slower overlying mantle and might be imaged as a slow anomaly in tomographic models. Thus there is the potential for feedback and bias when these models are used to compute travel time corrections to determine discontinuity depths from *SS* precursor data. Fortunately, as noted by *Revenaugh and Jordan* [1991] and *Shearer* [1993], this is only a second-order effect since reflected waves (such as the *SS* precursors) are much more sensitive to discontinuity topography than the transmitted waves used in the tomographic inversions. The probable error in the discontinuity depths introduced by using the tomographic models is proportional to $\Delta\beta/\beta$, where $\Delta\beta$ is the shear velocity contrast across the interface and β is the mean shear velocity. Using the PREM values for the contrast across the 660, discontinuity relief of 15 km will cause only a 1 km error in the corrections to the measured discontinuity depth. While ultimately a joint inversion for both boundary perturbations and velocity heterogeneity [e.g., *Vasco et al.*, 1995] is a desirable goal, we do not attempt such modeling here.

The timing corrections derived from CRUST5.0 and S16B30 have globally averaged mean values that are close to zero, so they have little effect on the mean discontinuity depths.

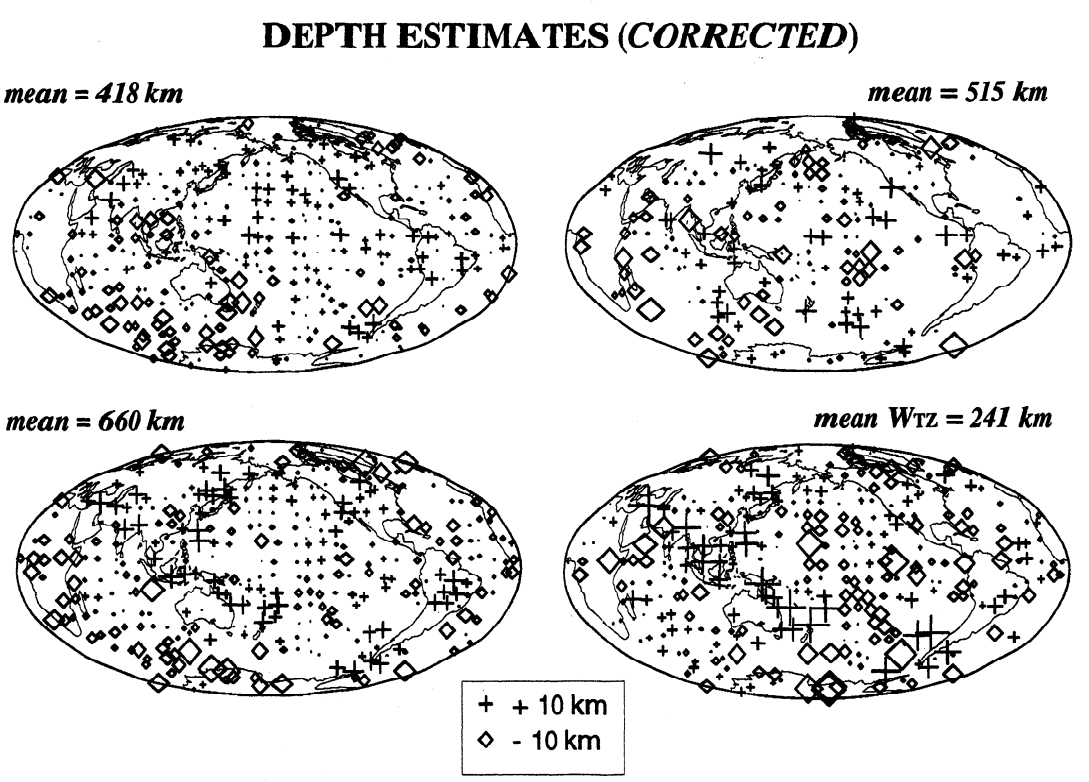

Figure 7. Map of the corrected depth estimates for the 410, 520, 660, and W_{TZ}, plotted at the cap locations as in Figure 5. These depths are computed after applying corrections for surface topography, crustal thickness, and upper mantle shear wave velocity structure beneath the *SS* bounce point. In addition, we apply a baseline shift to account for absolute *S* travel times through the upper mantle. The mean discontinuity depths are now slightly deeper than the raw depths seen in Figure 5.

However, this ignores the possibility that a systematic baseline difference could exist between predicted (model dependent) and observed *S* travel times through the upper mantle that would bias our absolute discontinuity depths. The S16B30 model was not designed to detect such a difference, as the *S* and *SS* travel times that went into the inversion were demeaned prior to analysis so as to concentrate only on the lateral velocity variations. To test for a systematic offset in the travel times, we examine 3458 long-period *SS-S* differential times at ranges between 65° and 95° (obtained from G. Masters (personal communication, 1996)). We bin these data by bounce point location using the same 416 bins used for our *SS* precursor analysis and compute residuals relative to PREM. Next, we apply corrections for the CRUST5.0 and S16B30 models, compute the median residual for the data within each bin, and then calculate the global median of the 293 caps that contain data. This yields an "average" residual for the *SS-S* observations of -3.3 s, indicating that actual *SS* times are significantly less than those predicted by ray tracing through the PREM + CRUST5.0 + S16B30 model. This timing offset is reduced to -2.95 at the *SS* precursor reference range of 138° due to the more vertical ray paths in the upper mantle at longer ranges. Applying this correction has a significant impact on our inferred absolute discontinuity depths, moving the discontinuities downward by about 8 to 10 km.

After applying all of the discussed adjustments, the new discontinuity depth estimates are mapped in Figure 7, together with the new global average depth for each discontinuity. Although the overall variance is slightly reduced, the large-scale patterns remain spatially coherent and the total range of values now spans 38 km for the 410 (398-436 km), 47 km for the 520 (490-537 km), 49 km for the 660 (633-682 km), and 69 km for W_{TZ} (210-279 km). The corrections have a significant effect on the 410 and 660 topography. For example, the magnitude of the trough along western North America appears greatly reduced, as does the trough in the eastern central Pacific ocean. There is also a reduction in 660 topography beneath China and Southeast Asia, and there are similar changes for the 410 in that same region. High-amplitude features of the 520 along the east Pacific Ocean margin and northernmost Canada are also reduced in magnitude, whereas W_{TZ} is changed little due to the small amplitude of the differential corrections between the *S*410*S* and *S*660*S* phases.

5. Observations of Global Topography

The global coverage provided by caps shown in Figure 7 is sufficiently complete that smooth maps of long-wavelength discontinuity topography can be constructed. We use the method of spherical splines to fit the individual cap values (including their standard errors) and then compute the equivalent spherical harmonic expansion of the splined field up to degree 12. This procedure penalizes short-wavelength structure as it minimizes the second lateral derivative integrated over the sphere, but examination of the amplitude or power spectra shows that most of the energy is below harmonic degree 12. We fit to χ^2 values that are representative

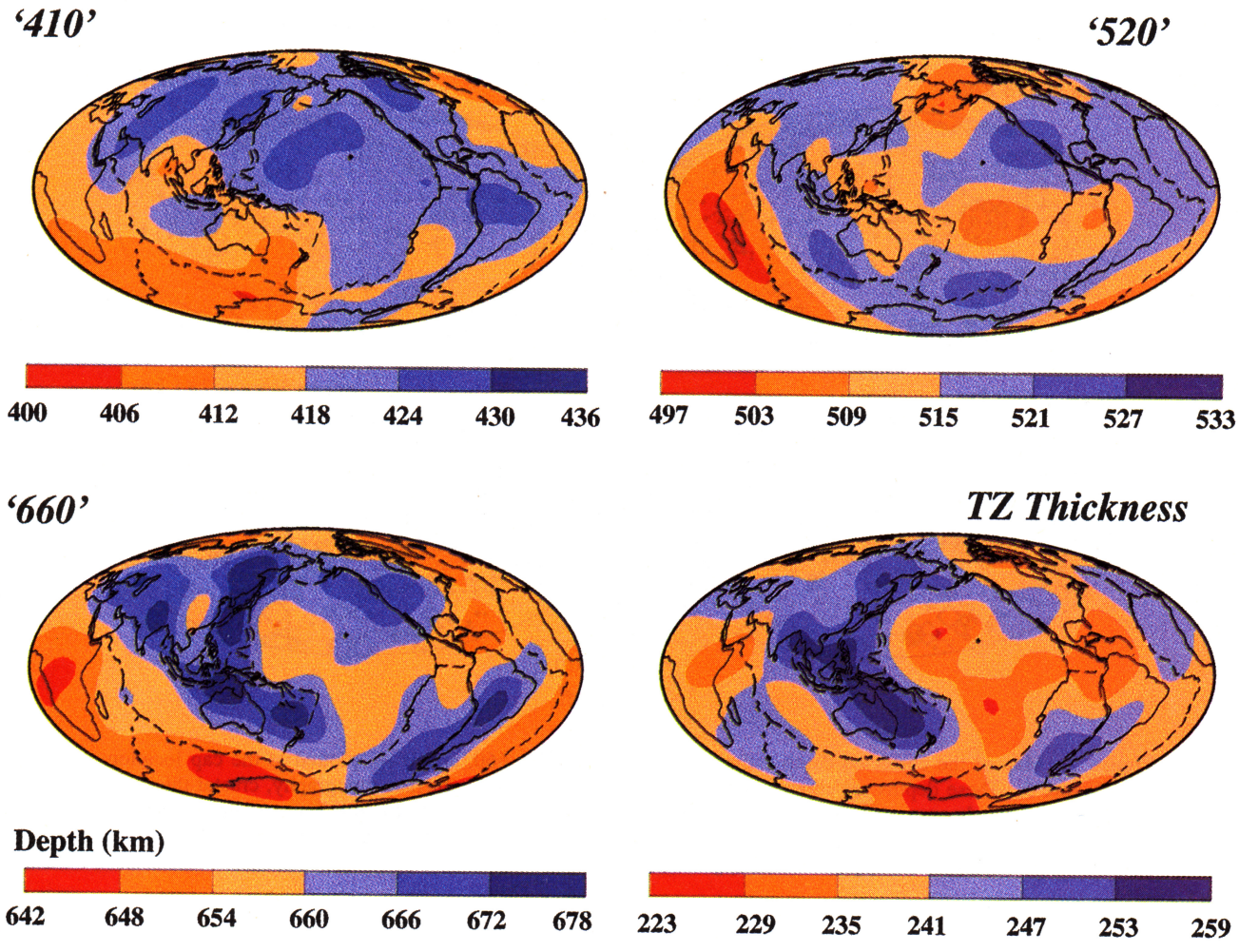

spherical splines applied to the cap averages shown in Figure 7. These maps are smoothed, interpolated fits to the depth estimates of each cap and are expressed as spherical harmonics up to degree 12. Contour intervals are 6 km; the dashed lines show the plate boundaries. Although the spherical spline method does not produce models with large structure in regions with no data, the topography should be viewed with caution in areas of poor data coverage.

of the number of caps in each inversion; χ^2 = 340 for the 410 and 660 topography, χ^2 = 200 for the 520, and χ^2 = 300 for W_{TZ}. Fitting to other χ^2 values mostly affects the peak-to-peak amplitude of the topography but does not significantly change the shape. The resulting smooth surfaces are mapped in Plate 2, and collectively these models are termed TOPOTZ. The spherical harmonic models provide a reasonable representation of the coherent topography visible in Figure 7, although some caution is warranted for the 520 map, since there are significant gaps in the data coverage where the results are unconstrained. The peak-to-peak topography in these models is 22 km for the 410 (406–428 km), 27 km for the 520 (500–527 km), 38 km for the 660 (643–681 km), and 35 km for W_{TZ} (222–257 km) with the same global averages as in Figure 7. (Depth and differential time values for the individual caps and the spherical harmonic coefficients for the smooth models are available from the authors via e-mail or ftp at mahi.ucsd.edu in the /pub/TOPOTZ directory.)

The new topography models seen in Plate2 exhibit both similarities and differences with the Topo410 and Topo660 models of *Shearer* [1993]. Many of the discrepancies occur in areas of sparse data coverage in the older models that are now better resolved; these regions include southeast Asia, the western United States, and Africa. However, there are also significant differences due to changes in the upper mantle velocity model used to correct the discontinuity depths. The current results correlate more closely with the previous topography models that were computed using the model SH8WM13 [*Woodward and Masters,* 1992], rather than model SH10C [*Masters and Bolton*, 1991]. This reflects the fact that the integrated upper mantle velocity anomalies in S16B30 are closer to those in SH8WM13 than to the earlier model SH10C (the current generation of long-wavelength, shear wave tomographic models is now in reasonable agreement; for this reason, we do not present results for a suite of different velocity models). Indeed, in a test producing topography models using upper mantle velocity corrections computed using the model of *Su et al.* [1994], there was no significant difference in the amplitude or pattern of the discontinuity topography relative to our models shown in Plate 2. The global average discontinuity depths are slightly greater than in *Shearer* [1993] (old, 413/653 km,; new, 418/660 km), with

much of this difference resulting from the corrections now applied for a baseline shift in the upper mantle S travel times (discussed in section 4 above). The possibility of a baseline offset was not accounted for by *Shearer* [1993]; thus the present results are more reliable.

5.1. The 660 Topography

The large-amplitude signals in the 660 topography are the most clearly resolved parts of the model. A particularly robust feature is a strong depression of the 660 observed in a ring around the Pacific Ocean, coincident with the location of actively subducting lithosphere, a result which supports the suggestion of *Shearer and Masters* [1992] that 660 depressions are correlated with subduction zones. This correlation is more apparent in TOPOTZ than in the models of *Shearer* [1993] due largely to changes in the model near Tonga and in the northeast Atlantic. These were areas which contained relatively few bounce points in the older model; the new results should be more reliable as we now have better data coverage in these regions as well as more complete corrections for crust and upper mantle structure. In addition to the 660 depressions associated with current subduction, there are depressions on this boundary that may be related to past subduction (i.e., western North America and southern Eurasia).

Recently, *Neele et al.* [1997] questioned the validity of inferring large-scale discontinuity topography from long-period underside reflections in areas where significant small-scale topography is present. They computed synthetic seismograms using Kirchhoff theory for precursors to PP resulting from reflections off discontinuities at 420 and 660 km ($P420P$ and $P660P$). For the northwest Pacific, they examined a discontinuity topography model with narrow (4° wide), 50-km-high ridges on the 410 and 50-km-deep valleys on the 660, both aligned with the position of the subducting slabs. They found that long-period synthetic seismograms, produced using the same distribution of sources and receivers as the SS precursor study of *Shearer* [1993], yield discontinuity topography models that are biased. This results from the interaction of narrow topographic anomalies with the large, saddle-shaped Fresnel zones of the PdP phases. In particular, Neele et al. suggest that the large depression in the 660 topography in the northwest Pacific observed by *Shearer* [1991, 1993] and *Shearer and Masters* [1992] may be an artifact.

Neele et al. [1997] raise an important issue: the degree to which large-scale maps of discontinuity topography inferred from long-period reflections may be biased by small-scale structure. However, it is not clear if their results provide a reliable guide to the validity of this and previous SS precursor studies for two reasons: (1) They model PdP rather than SdS arrivals, and (2) the dominant period of their synthetic reference pulses is about 15 s, while the topography models are derived from data of about 30-s period. Other evidence suggests that the observed 660 depressions near subduction zones are real. The artifacts predicted by Neele et al. are symmetric and centered on the slab anomalies, whereas the depressions observed in Figure 7 and Plate 2 are displaced to the west of the slabs. Their model predicts similar artifacts in both the 410 and 660 topography, but our observed 410 topography is uncorrelated with subduction zones and with the 660 topography. The position of the observed 660 depression in the northwest Pacific is correlated with fast velocity anomalies in the transition zone seen by *van der Hilst et al.* [1993] and *Ding and Grand* [1994] and is consistent with the ScS reverberation analysis of *Revenaugh and Sipkin* [1994]. Nonetheless, it is important to consider the effect of small-scale topography on our results, and in future work, we hope to address the questions raised by *Neele et al.* [1997] more directly by applying back-projection and Kirchhoff migration techniques to SS precursor data. Such an analysis may also help to resolve additional localized and/or dipping reflectors [e.g., *Castle and Creager*, 1996; *Weber and Wicks*, 1996] that are not coherent enough to be imaged in the cap-averaging scheme adopted here (which is analogous to common-midpoint stacking in reflection seismology).

The observation of broad depressions in the vicinity of subducting slabs is consistent with models in which subducted material spreads out or "lays down" on the 660-km discontinuity, thus spreading the cold slab temperatures into the adjacent mantle. The apparent deflection of slabs could result from resistance to slab penetration across the 660 phase change, as suggested by *Ringwood and Irifune* [1988] and numerical convection simulations [*Machetel and Weber*, 1991; *Peltier and Solheim*, 1992; *Tackley et al.*, 1993; *Honda et al.*, 1993]. This idea is supported by recent tomographic inversions of several subduction zones which image horizontal extensions of the slab just above 660-km depth [*Fukao et al.*, 1992; *Ding and Grand*, 1994; *van der Hilst*, 1995; *Bijwaard et al.*, 1996]. Our results indicate that the largest 660 depressions (about 20 km) occur beneath the Japan and Kuril slabs, west of the Izu-Bonin slab, west of the Tonga trench, and under South America, whereas more moderate depressions (about 10 km) are seen below the Philippine and Java trenches. Uplift of the 660 is observed beneath Africa, Antarctica, and the southern Atlantic Ocean. Recent P wave tomographic images of several subduction zones produced by *van der Hilst et al.* [1991] reveal a variety of interactions of slabs with the 660-km discontinuity. Beneath the Izu-Bonin and the southern part of Japan trenches in the northwest Pacific and beneath the northern Tonga trench in the southwest Pacific, the slab seems to be deflected along the boundary to the west for a few hundred kilometers, and in Tonga, it then continues downward into the lower mantle. Beneath the Marianas and northernmost Kuril-Kamchatka trench the slab appears to penetrate the boundary, reaching depths of 1000 km or more. This suggests that the extent of the depression of the 660 may be controlled by the slab behavior; where slabs go through the 660, we observe only slight depressions in the 660; where slabs are recumbent on this discontinuity, we observe about a 20-km depression of the boundary.

This same combination of part deflection and part penetration has also been observed along the strike of other subducted slabs. The Tonga slab is deflected at the northern end of the trench and penetrates the 660 in the southern Kermadec trench [*van der Hilst*, 1995]. In South America the slab penetrates beneath the north region of the continent and is recumbent beneath the central part [*Engdahl et al*, 1995], while in the Java-Banda trench the slab is deflected in the east beneath Banda and appears penetrating or possibly detached toward the west under Java-Sumatra [*Widiyantoro and van der Hilst*, 1996]. In addition, new high-resolution global tomography models by *van der Hilst et al.* [1997] (P wave) and *Grand et al.* [1997] (S wave) show several slab-like features at

midmantle depths of 600-1700 km not only beneath current subduction zones but beneath areas of previous subduction, e.g., the Americas (Farallon plate) and southern Eurasia (Tethys Sea plate).

Regional studies of discontinuities near subduction zones using near-source *S* to *P* converted waves have found evidence for slab-induced depressions of 20-30 km on the 660-km discontinuity under Tonga [*Richards and Wicks,* 1990; *Niu and Kawakatsu,* 1995] and up to a 60-km depression beneath Izu-Bonin [*Wicks and Richards,* 1993; *Castle and Creager*, 1996]. *Vidale and Benz* [1992] obtained depth perturbations of up to 30 km beneath the Tonga, Izu-Bonin, Marianas, and South American subduction zones. These studies have much higher resolution in the immediate vicinity of the subducting slabs than our *SS* precursor observations but are in good general agreement with our results concerning the location and magnitude of depressions of the 660-km discontinuity (Plate 2). A notable exception to this consensus is the *SS* precursor study of *Petersen et al.* [1993], who found an elevation of the 660 in the northwest Pacific Ocean of 10 to 20 km, in disagreement with the well-resolved trough seen in Plate 2. This discrepancy is likely due to the small number of data examined by *Petersen et al.* [1993] and the contrived grouping of the bounce points used in their study which encompass a region over 50° wide (including areas well outside of the subduction zone).

5.2. The 410 Topography

Just as the 660 phase boundary is depressed in cold regions, the 410 is expected to be elevated near cold subducting lithosphere. However, we do not observe significant elevations of the 410 near subduction zones; rather, it seems to be within 5 to 6 km of the global average (and slightly depressed) near the Tonga, South America, and the northwest Pacific subduction zones. Tomographic images of subduction zones exhibit slow velocities in the backarc regions to depths of 300 and 400 km [*van der Hilst et al.*, 1991] which can be interpreted as areas of warmer temperature, so the 410 may be slightly depressed beneath backarc basins relative to the global mean. The phase transitions in olivine at 410 km depth can be deflected upward in the cold interior of slabs, but this should occur quite narrowly [*Bina and Helffrich*, 1994]. Moreover, the pyroxene to garnet phase transitions will amplify negative buoyancies near 410 km but at longer wavelengths than the olivine polymorphism [*Bina and Wood*, 1984; *Akaogi et al.*, 1987]. Seismic observations of the upward deflection of the 410 near slabs have been made [*Vidale and Benz,* 1992; *Zhang and Lay*, 1993; *Flanagan and Shearer,* 1997; *Collier and Helffrich*, 1997]. However, this effect is likely confined to within the slab itself as well as the immediate surrounding mantle, comprising a narrow zone of uplift less than a few hundred kilometers wide and not a broad regional signature resolvable with the long-period *SS* precursors. Our observations suggest that the horizontal slab deflections that produce the large regional depressions seen in the 660-km discontinuity do not significantly affect the 410-km phase boundary; the cold material that accumulates above the 660-km interface does not extend up to 410 km.

Topography on the 410 appears to have little correlation to any surface tectonic features (Plate 2). There is no particular thinning of the transition zone beneath ridges; instead the transition zone width is dominated by the 660 topography due to its higher amplitude relative to the 410 topography. Recent observations of the 410 and W_{TZ} in the regions beneath ridges and hotspots are somewhat contradictory. *Lee and Grand* [1996] in a study of *SS* precursors beneath the East Pacific Rise (EPR) observe no significant depression of the 410 or thinning of the transition zone below the ridge and no correlation of 410 topography and age of ocean floor between 0 and 30 Ma. They report a 0–3 km difference in transition zone thickness relative to the global average for oceans and conclude that deep upwelling beneath the northern EPR, if it exists at all, must be near the average adiabatic temperature gradient for the Earth and thus appears to be an essentially passive phenomenon. *Shen et al.* [1996] in a study of *P* to *S* conversions beneath Iceland find a transition zone 23 ± 9 km thinner than iasp91 (W_{TZ} = 250 km) but cannot distinguish whether this is due to a deeper 410, a shallower 660, or both. This observation of a thin transition zone beneath Iceland may be related to the intersection of a hotspot and spreading ridge, but the region of their study is 200 to 300 km wide, and it may not be possible to detect this local anomaly in our study. Indeed, it is likely that deflections of transition zone topography beneath hotspots may occur on scales of only a few hundred kilometers, in contrast with the apparently large-scale signature of many subduction zones. Similarly, the short scale-length topography on the 410 recently observed by *Dueker and Sheehan* [1997] from *P*-to-*SV* converted arrivals in the western United States would not be resolvable with our data.

Jordan [1975] and *Lerner-Lam and Jordan* [1987] introduced the idea of a tectosphere: that old cratons have cold deep roots or "keels" which extend 200 to 300 km into the upper mantle. A recent *SS* precursor study of *Gossler and Kind* [1996] suggested that on average, the transition zone is 14 km thicker beneath continents than beneath oceans, and *Gu and Dziewonski* [1996], also examining *SS* precursors, report that the average depth of the 410 is about 5 km less on continents compared to oceans. Both results suggest that the cold thermal anomalies associated with continental roots may extend to at least 410 km, which would have important implications for continental structure and mantle convection.

However, our observations indicate no clear correlation between 410 topography or transition zone thickness and the location of oceans and continents; under some continents the 410 is elevated (Africa, Australia, Europe), beneath others it is depressed (North and South America), and beneath some it is both (Asia, Antarctica). This is evident in the smooth maps in Plate 2, but is further demonstrated by plotting the individual depth estimates from each cap divided into ocean and continent histograms (Figure 8). We find the average depth of the 410 is 417 km beneath oceans and 419 km beneath the continents, and the mean thickness of the transition zone is 241 km beneath continents and 240 km beneath oceans. These differences are not statistically significant given the scatter in the individual histograms. Thus our results indicate that transition zone discontinuity depths are not measurably impacted by ocean/continent differences; any thermal anomaly associated with deep continental roots is overwhelmed by much larger lateral variations in temperature that are uncorrelated with the locations of continents. This interpretation is supported by a recent study of *P*-to-*SV* converted phases beneath eastern North America [*Li et al.*, 1996], which finds no significant differences in mantle discontinuity depths across the margin of the high-velocity continental root. *Revenaugh and Jordan* [1991] in their *ScS*

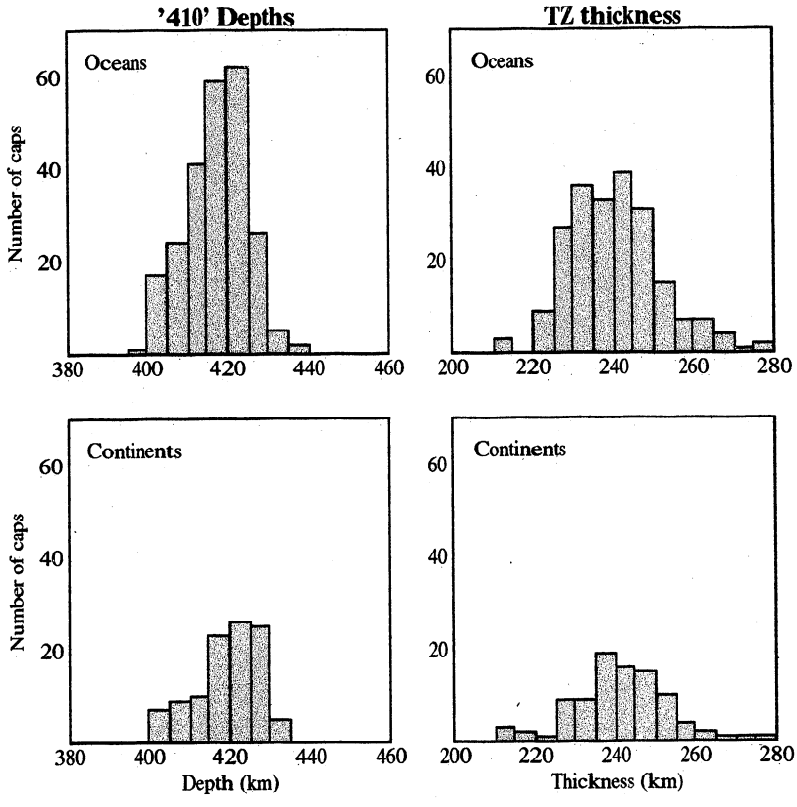

Figure 8. Histograms of depth estimates for the 410-km discontinuity and the transition zone thickness divided into oceanic and continental caps; standard error criterion is <10 km for the 410 and <15 km for the transition zone thickness. The mean depth of the 410 is 417 km beneath oceans (237 caps) and 419 km beneath the continents (103 caps), while the mean thickness of the transition zone is 240 km beneath oceans (214 caps) and 241 km beneath continents (92 caps). This similarity indicates no significant ocean-continent signal in the discontinuity topography.

reverberation studies of several ocean-continent margin paths also observe a lack of correlation between W_{TZ} and surface tectonics.

Given this consistency, why do our results disagree with those of *Gossler and Kind* [1996] and *Gu and Dziewonski* [1996] since their studies are also based on *SS* precursor observations? The transition zone thickness map reported by *Gossler and Kind* [1996] is roughly similar to our results but uses a coarser binning scheme (30° by 30° cells) and has more limited spatial coverage, particularly on the continents. The ocean/continent difference that they observe is largely due to increased transition zone thicknesses seen in western Asia (agreeing with our results) and northern North America (disagreeing with our results); their mapping excludes areas such as Antarctica (where we see a thinner transition zone) and the southwest Pacific (where we see a thicker transition zone). Thus it appears likely that their observed ocean/continent difference may be largely due to random chance and the incomplete global coverage of their data. The 5-km ocean/continent difference reported by *Gu and Dziewonski* [1996] is based upon a global study similar in scope to ours. Here, the difference may lie in the corrections for crust and upper mantle structure, which have a strong ocean/continent signal (e.g., see Figure 6). Any uncertainty in these corrections is likely to imprint an ocean/continent signal onto the absolute discontinuity depths. For this reason, the transition zone thickness provides a more reliable way to assess ocean/continent differences in discontinuity depths, albeit with less direct sensitivity to the 410 alone.

5.3. The 520 Topography

The results for the 520-km discontinuity are intriguing but incomplete; the 520 is resolved in approximately half of the global caps, much less than the coverage for the 410 and 660. To what extent does this difference reflect actual brightness variations in the 520 reflector, compared to variations in its detection due to the low signal-to-noise of the *S520S* phase? The 520 impedance contrast is less than half that seen for the 410 [e.g., *Revenaugh and Jordan*, 1991; *Shearer*, 1996]; this is apparent in the waveform stacks where the 520 peak has a relatively low amplitude. However, the visibility of the 520-km peak improves as the number of data in the stack increases. This is demonstrated in Figure 9, histograms of the number of caps that have visible 520 peaks as a function of the number of traces in the cap. The fraction of caps with clear 520 peaks increases as the number of data grows larger. The 520 is observed in every case where more than 250 traces comprise the stack, regardless of whether continental or oceanic bounce points are considered. Thus the absence of a clear 520-km peak in *SS* precursor observations is not necessarily evidence against the presence of the 520 in that particular region. It seems more plausible that the 520 is a global feature that cannot always be reliably observed unless large numbers of seismograms are available to stack. This provides an alternative explanation for the results of *Gossler and Kind* [1996], who concluded from their *SS* precursor study that the 520 is only a regional reflector. The existence of a global 520-km discontinuity is also supported by the *ScS*

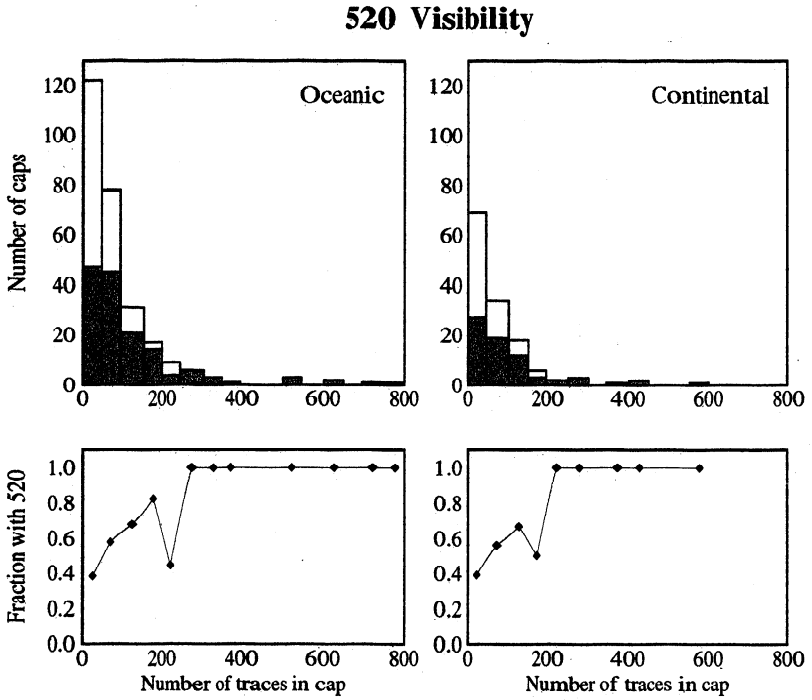

Figure 9. Histograms showing the visibility of the 520-km discontinuity beneath oceans (135 caps) and continents (64 caps) as a function of the number of traces in each cap. Open boxes represent the total number of caps containing 10 or more seismograms; shaded boxes show the number of caps with a clear 520 peak and an estimated standard error in depth of 15 km or less. The visibility of the 520 decreases when fewer data are available to stack.

reverberation study of *Revenaugh and Jordan* [1991], who observed the 520 under a variety of oceanic and continental margin paths, and is consistent with the properties of the pressure-induced phase change from β to γ spinel that is expected near 520 km depth from mineral physics experiments [e.g., *Rigden et al.*, 1991]. However, a definitive result concerning the ubiquity of the 520 will not be possible from *SS* precursor observations until more data become available for those sparsely sampled regions where the 520 is only intermittently observed.

The low signal-to-noise of the *S*520*S* observations also hampers reliable measurements of possible topography on the discontinuity. Figure 10 shows the calculated standard errors in depth for the 410-, 520- and 660-km discontinuities as a function of the number of records in the cap. For the same number of records, higher errors are associated with the 520 observations. The 410 and 660 have clear, sharp peaks and small standard errors even when there are as few as 10 or 20 seismograms in the cap. Observations of the 520 are more variable: for example, the caps containing 50 to 100 records have a wide range of error estimates depending on the amplitude and sharpness of the 520 peak, as our stacking procedure computes standard errors even when there is no sharp peak in the waveform stack. Fewer reliable depth estimates are obtained for the 520 than for the 410 and 660 (Figure 7), and the smoothed map of discontinuity topography should be considered less reliable due to the larger gaps in spatial coverage. Despite these limitations, some features appear to be resolved, including highs in the north and south central Pacific and a depression in the mid-Pacific (see Figures 3, 7 and Plate 2).

6. Interpretation of Topography

The topography on the transition zone discontinuities provides valuable information regarding the structure, temperature, and dynamics of the mantle. Modeling results have shown that a compositional boundary at 660 km associated with layered convection would be displaced several hundred kilometers or more by subducting slabs [e.g., *Hager and Raefsky*, 1981; *Christensen and Yuen*, 1984]. Subsequent observations that the amplitude of 660 topography is of the order of tens of kilometers provide strong evidence against a purely compositional origin for the 660-km discontinuity [e.g., *Revenaugh and Jordan*, 1991; *Shearer*, 1991]. It is now generally accepted that most, if not all, of the velocity and density changes across the 410- and 660-km discontinuities result from phase changes, which mineral physics experiments predict will occur near these depths. Thus variations in discontinuity depths should provide constraints on mantle temperatures, to the extent that the P-T relationships for the appropriate phase changes are known from mineral physics experiments. Topography on the 660-km discontinuity also plays a major role in mantle dynamics, as the endothermic phase transition at 660 km depth acts to inhibit thermally driven flow across the interface. Recent numerical convection experiments have indicated that a relatively steep Clapeyron slope for the 660 may prevent direct slab penetration and result in partially layered convection [e.g., *Machetel and Weber*, 1991; *Peltier and Solheim*, 1992; *Tackley et al.*, 1993; *Honda et al.*, 1993].

We now consider three features of the TOPOTZ model: (1) the relative amplitude of the 410 and 660 topography, (2) the lack of correlation between the 410 and 660 topography, and

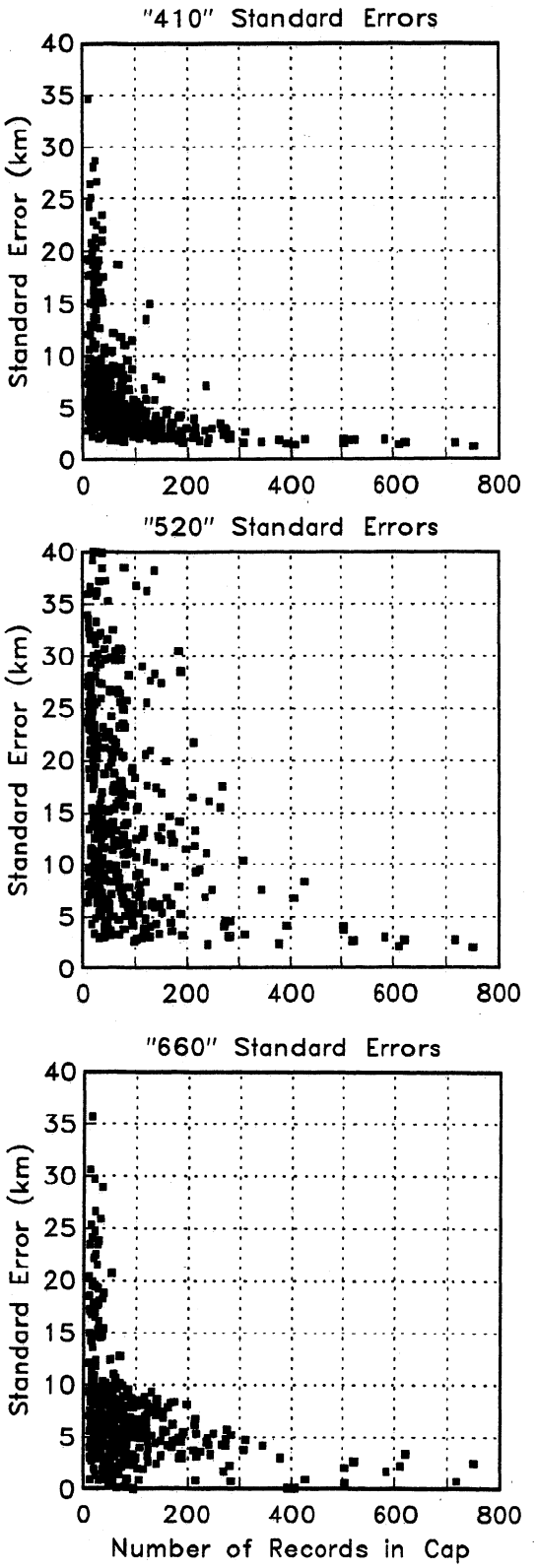

Figure 10. Standard errors of the depth estimates for the 410-, 520-, and 660-km discontinuities measured from each bounce point cap, plotted as a function of the number of seismograms in the cap. These errors are computed using a bootstrap technique of randomly resampling the records in each cap prior to stacking. The 410 and 660 depth estimates have low standard errors when there are sufficient data in the cap, while the 520 depth estimates have greater errors for the same number of data (the highest errors are off the scale of the plot and extend to 61 km for the 520).

(3) the relationship between discontinuity topography and shear velocity perturbations in the S16B30 tomography model.

6.1. Greater Topography for the 660 than the 410

One of the most striking features of model TOPOTZ is that larger-amplitude topography is observed on the 660 relative to the 410, a result which cannot be explained by inadequacies in the crustal and upper mantle velocity corrections or by the formal errors in our measurements. In Figure 11 we plot the standard errors against the depth variations of the 410, 520, 660, and W_{TZ} (these are the corrected depth estimates). Note that the 40 to 45 km peak-to-peak variation in the 660 topography is clearly larger than the 30 to 35 km variation in the 410 topography, even for the measurements with the smallest standard errors. This is consistent with previous analyses [*Shearer*, 1991, 1993] and is one of the most robust features of mantle discontinuity observations.

To infer mantle temperature variations from these results, one needs values for the appropriate Clapeyron slopes. Unfortunately, data on this subject from both experiments and thermodynamic calculations are somewhat conflicting with a wide range of estimates for both the 410 and 660 phase boundaries. Values obtained for the α to β spinel phase change at 410 km vary from $dP/dT = 1.5 \pm 0.8$ MPa/°K [*Akaogi et al.*, 1989], $dP/dT = 2.5$ MPa/°K [*Katsura and Ito*, 1989], $dP/dT = 2.7$-2.9 MPa/°K [*Chopelas*, 1991], to $dP/dT = 2.9$ MPa/°K [*Bina and Helffrich*, 1994]. For the γ spinel to perovskite and magnesiowüstite reaction at 660 km, values range from $dP/dT = -2.0$ MPa/°K [*Ito and Yamada*, 1982], $dP/dT = -2.8$ MPa/°K [*Ito and Takahashi*, 1989], $dP/dT = -4.0 \pm 2.0$ MPa/°K [*Ito et al.*, 1990], $dP/dT = -3.0$ MPa/°K [*Akaogi and Ito*, 1993], to $dP/dT = -2.1$ MPa/°K [*Bina and Helffrich*, 1994].

If the lateral temperature variations at 410 km are assumed equal in amplitude to those at 660 km, then our results would indicate that the Clapeyron slope for the 660 is probably steeper than that for the 410. This was the preferred interpretation given by *Shearer* [1991, 1993], who suggested that the greater topography observed on the 660 favored the *Akaogi et al.* [1989] and *Ito et al.* [1990] results. However, recently, *Bina and Helffrich* [1994] examined this issue, reviewing the mineral physics results to date, and argued that the 410 Clapeyron slope is larger in magnitude than the 660 and that the origin for the higher observed topography on the 660 must lie elsewhere. They discuss several alternative explanations, including the possibility that lateral temperature variations near 660 km are greater than those at 410 km or that larger topographic variations on the 410 are masked in some way from seismic observations. Our results argue against the latter explanation since the 410 reflector is clearly observed over most of the Earth's surface and provides depth estimates with standard errors that are no larger than those observed for the 660 (see Figure 11). Larger temperature anomalies might be expected near 660 km than near 410 km, at least at long wavelengths, due to the inhibiting effect of endothermic phase changes on thermally driven flow. This would go against the general trend of decreasing lateral heterogeneity with depth in the upper mantle seen in recent whole mantle tomography models [e.g., *Su et al.*, 1994; *Masters et al.*, 1996], but it is possible that these models do not have the vertical resolution to reliably resolve relatively thin anomalies near 660 km. A possible complication in the interpretation of 410 topography simply in terms of a

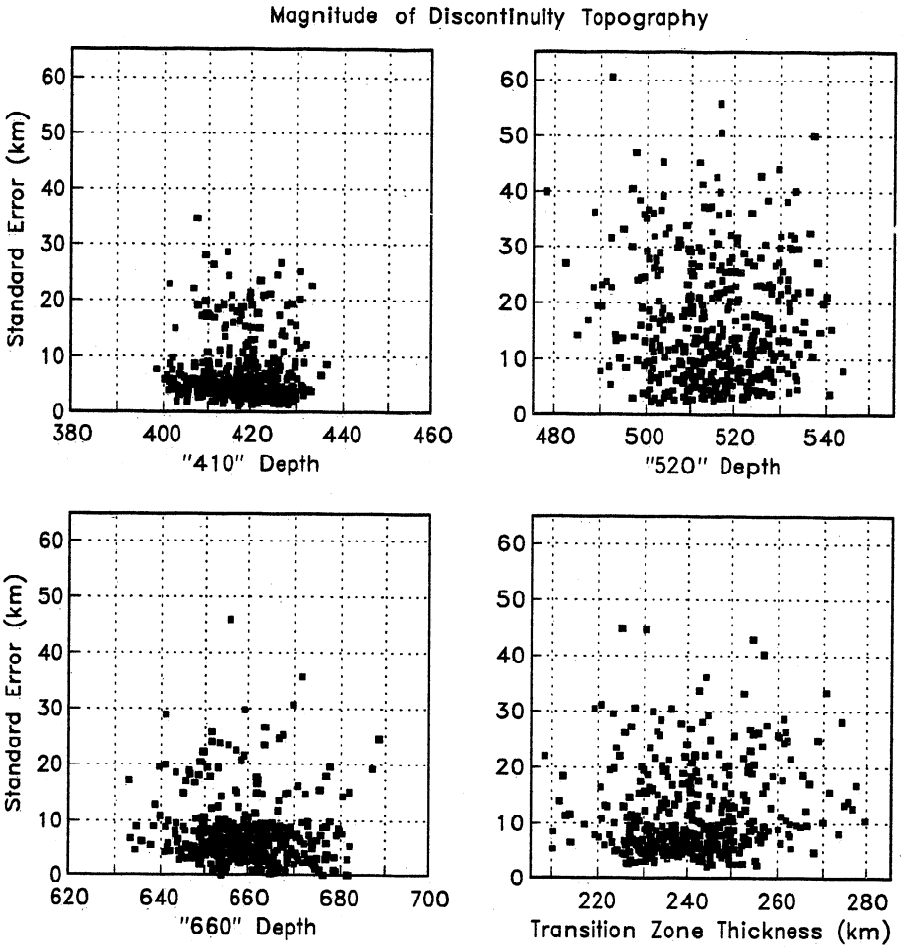

Figure 11. Standard errors plotted against the magnitude of the depth variation of 410, 520, 660, and transition zone thickness. These depth estimates have been corrected for surface topography, crustal structure, and upper mantle velocity structure. Note the greater peak-to-peak depth variation of the 660 relative to the 410, even at small standard errors.

Clapeyron slope involves the fact that the velocity increase across the α to β phase transition is not expected to be linear [e.g., *Helffrich and Wood*, 1996; *Stixrude*, 1997] and the shape of the phase loop is temperature dependent.

Finally, we note that our observations suggest the magnitude of topography on the 520-km discontinuity is greater than that on the 410, consistent with a steeper Clapeyron slope for the 520 [*Katsura and Ito*, 1989; *Brearley et al.*, 1992; *Ita and Stixrude*, 1992; *Rubie and Brearley*, 1994], but at least some of the observed difference may be due to the larger uncertainties in the 520 depth estimates (see Figure 11).

6.2. Uncorrelated 410 and 660 Topography

If temperature anomalies within the transition zone are vertically coherent, then topography on the 410 and 660 discontinuities should be negatively correlated due to the opposing signs of their Clapeyron slopes. The discontinuities should move closer together in warm regions and farther apart in cold regions. *Revenaugh and Jordan* [1991] found marginal evidence for such a negative correlation from *ScS* reverberation data. *Stammler et al.* [1992] and *Bostock* [1996] observed a positive correlation using observations of *P*-to-*SV* converted phases (*P*410*s* and *P*660*s*) but noted that this correlation probably results from the effect of overlying crust and mantle heterogeneity on their *Pds* - *P* differential time measurements. In our study, we attempt to account for this effect by applying corrections for shallow structure; these corrections play a critical role in comparisons of 410 and 660 topography, since either undercorrecting or overcorrecting the data for heterogeneity above the 410 can introduce spurious correlations between 410 and 660 depths.

Our results suggest that the 410 and 660 depths are, to first order, uncorrelated (see Plate 2), implying that the assumption of vertically coherent temperature anomalies between the 410 and 660 is simplistic. For example, there appear to be large regional depressions in the 660-km discontinuity associated with subduction zones with no corresponding regional elevations of the 410-km discontinuity. As discussed above, this is to be expected if the slabs pass through the 410 relatively undeformed, producing a narrow elevation of the 410 that is unobservable in the long-period *SS* precursor data, whereas slab deflection near 660 km depth produces much more extended thermal anomalies. One should, of course, expect some correlation between thermal anomalies near 410 and 660 which would consequently produce some anticorrelation in the topography; however, this is probably counterbalanced to some degree in our results by inadequacies

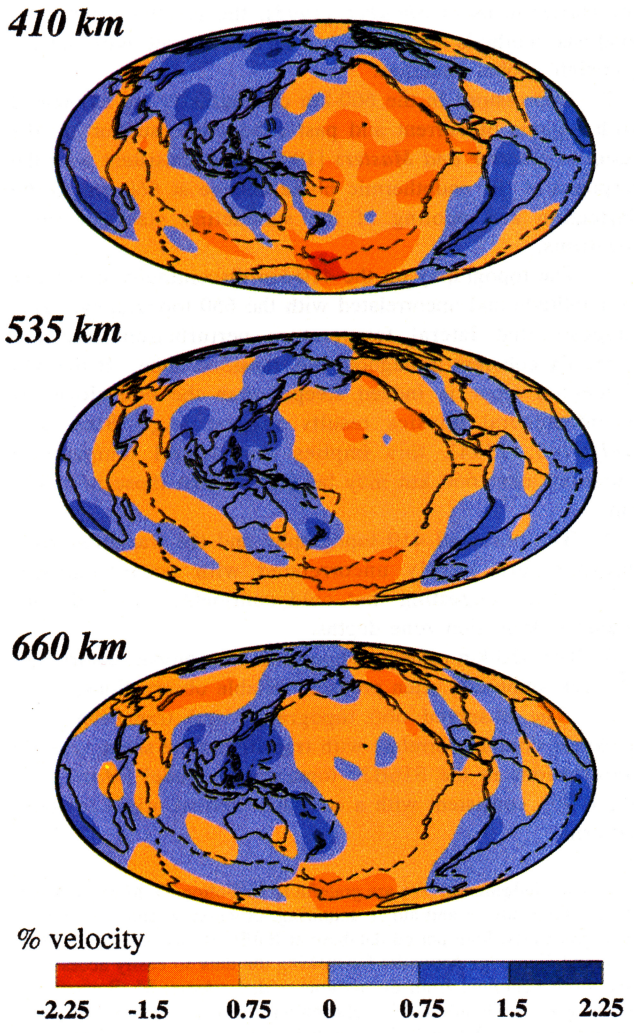

Plate 3. Maps of shear wave velocity anomalies in percent at depths of 410, 535, and 660 km from the mantle tomography model S16B30 [*Masters et al.*, 1996] with faster velocities shown in blue and slower velocities shown in red. The velocity perturbations at 535 and 660 km roughly correlate with the transition zone thickness and 660 topography maps in Plate 2, suggesting a common thermal origin (i.e., a cool region has faster velocities, a deeper 660, and a wider transition zone).

in the corrections for shallow structure. Since a quantitative assessment of the relative size of these effects is difficult, perhaps a more fruitful approach is to compare discontinuity depths with another observed parameter, the velocity anomalies in the transition zone seen in tomographic models.

6.3. Velocity Anomalies in the Transition Zone

Maps of shear wave velocity anomalies at depths of 410, 535, and 660 km from S16B30 [*Masters et al.*, 1996] are shown in Plate 3 for comparison with the TOPOTZ discontinuity topography models in Plate 2. Velocity perturbations are shown in percent, with blue indicating faster, presumably colder regions, and red indicating slower, presumably warmer, regions. The velocity anomalies are strongly correlated between the three depths, with all of the maps showing a rough correlation with both the 660 topography and the transition thickness maps. This is consistent with the expected behavior of an endothermic phase change at 660 km, with depressions in the 660 associated with cold, fast velocity anomalies. However, the observed 410 topography does not agree with the S16B30 velocity anomalies at 410 km, as elevations in the 410 are not generally associated with faster regions in the tomography model. The map of velocity perturbations at 410 km shows a strong ocean/continent signal; as discussed above in section 5.2, the 410 topography does not exhibit such a signal. The most likely explanation for the discrepancy at 410 is that the limited vertical resolution of the tomographic model results in a vertical smearing of the velocity anomalies through the transition zone and that the ocean/continent signal seen in the

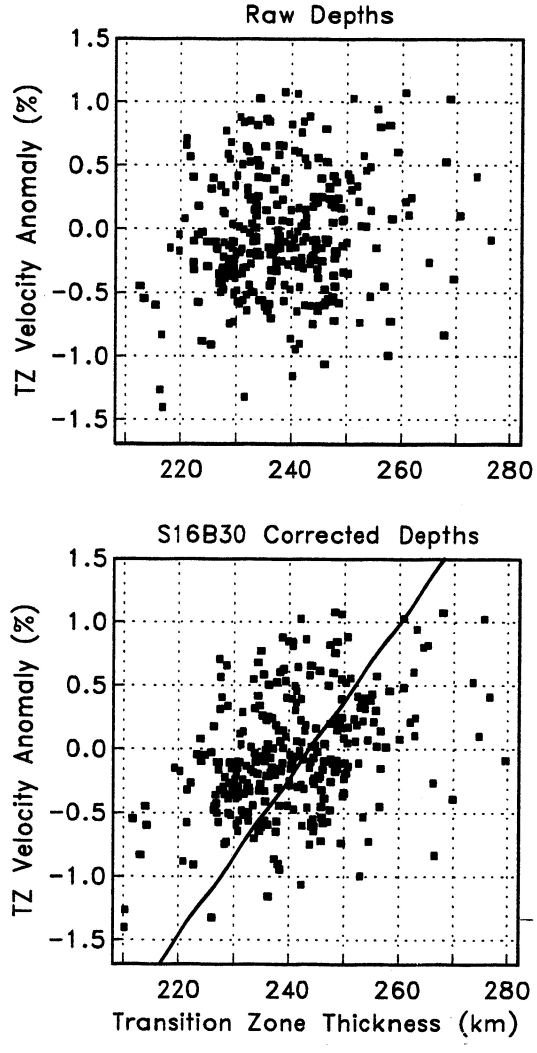

Figure 12. Transition zone shear velocity anomalies in percent from the mantle tomography model S16B30 of *Masters et al.* [1996] versus raw and corrected transition zone thickness estimates for the 306 caps plotted in Figures 5 and 7. The rough positive correlation seen in the bottom plot is consistent with thermally induced topography on the 410 and 660 discontinuities indicated by the opposite signs for the Clapeyron slopes of mineral phase transformations at those depths. The solid line indicates the theoretical prediction for vertically coherent temperature anomalies in the transition zone, assuming $d\beta/dT$ = -0.44 m/s°K and values of 3 and -2 MPa/°K for the 410 and 660 Clapeyron slopes (see text).

velocity anomalies at 410 km is leakage from fast continental roots at shallower depths.

In principle, the discontinuity topography observations provide a constraint on the mantle temperatures locally at the depth of the discontinuities. In contrast, the tomography models necessarily have some degree of vertical smoothing and provide a measure of the temperature averaged over some depth interval. Thus, depending upon the degree of vertical coherence in mantle temperature perturbations, we should not expect to see a perfect correlation between the observed topography and the tomographic results at the same depth. The fact that the observed 410 and 660 topographies are essentially uncorrelated indicates that the vertical scale length of temperature perturbations in the transition zone is significantly shorter than 250 km (there is also a lack of correlation between the observed 410 and 520 topography, suggesting an even shorter vertical scale length, but this is not as reliable as the 410/660 comparison, given the larger errors and gaps in the 520 depth estimates). This suggests that the highly correlated velocity perturbations at 410 and 660 km in S16B30 are largely imposed by the smoothing in the model.

The uncertainties in the tomographic models associated with their limited vertical resolution can be reduced by averaging over a given depth interval. In Figure 12, we plot the vertically averaged shear velocity perturbation in the S16B30 model between 410 and 660 km against the transition zone thickness W_{TZ} at each of the caps for which the standard error of W_{TZ} is less than 15 km. A weak positive correlation is shown, with fast velocities associated with a thicker transition zone and slower velocities associated with a thinner transition zone. If we assume values for the Clapeyron slopes and a shear velocity-temperature scaling relationship, we can compare these results to theoretical predictions. The solid line shown in Figure 12 was computed assuming $d\beta/dT$ = -0.44 m/s°K [*Revenaugh and Jordan*, 1991], with values of 3 and -2 MPa/°K for the 410 and 660 Clapeyron slopes, respectively (values close to those of *Bina and Helffrich* [1994]). This theoretical curve appears somewhat steeper than the data; it could be adjusted to provide a better fit either by increasing the difference in the Clapeyron slopes or decreasing the value of $d\beta/dT$. Of course, a perfect fit is not to be expected since much of the scatter shown in the plotted points probably results from vertical structure in the mantle temperature perturbations as well as errors in both the discontinuity depths and the tomography model. Ultimately, one would hope to develop internally consistent models of Earth structure in which a thermal model of the mantle could be constructed that would predict, through appropriate scaling relationships, a model of discontinuity topography and three-dimensional volumetric velocity perturbations that would satisfy both the discontinuity reflection data used in this study and the travel time and normal mode data used to construct the tomographic models.

7. Summary

The principal results of this work are summarized as follows:

1. New maps of topography on the 410-, 520-, and 660-km discontinuities, constructed using long-period *SS* precursor observations, reveal large-scale coherent depth variations. Our TOPOTZ models represent a significant improvement over the earlier maps of *Shearer* [1993], the result of improved analysis methods applied to a larger dataset with nearly complete global coverage.

2. Depressions in the 660-km discontinuity are associated with regions of current and past subduction, supporting the result of *Shearer and Masters* [1992], and consistent with the response of the endothermic phase change at 660 km to the deflection and pooling of the subducting slabs in some locations.

3. The topography on the 410-km discontinuity is smaller in amplitude and uncorrelated with the 660 topography. This suggests that lateral temperature perturbations are not vertically coherent throughout the transition zone. If the 410 Clapeyron slope is indeed steeper than the 660 slope, as recent mineral physics results suggest [e.g., *Bina and Helffrich*, 1994], this implies that lateral temperature variations near 660 km may be greater than those near 410 km.

4. The observed 410 topography and the transition zone thickness are largely uncorrelated with ocean/continent differences, suggesting that cold continental roots do not extend to transition zone depths.

5. The 520-km reflector appears to be a global feature, but its weak amplitude often prevents reliable observations.

6. The observed 660 topography and transition zone thickness crudely correlate with transition zone shear velocity perturbations in the S16B30 tomography model [*Masters et al.*, 1996], consistent with a common thermal origin for both patterns.

Acknowledgments. We are grateful to H. Bolton, G. Masters, and J. Um for their advice and aid in acquiring, processing, and maintaining the high-quality, long-period database at IGPP; we also thank the IRIS, IDA, and Geoscope networks for making the data so easily accessible. This work benefited from discussions with L. Astiz, M. Bostock, A. Dziewonski, S. Grand, and S. Johnson and from critical and insightful reviews from G. Helffrich, M. Kendall, and one anonymous reviewer. We thank G. Anderson, L. Astiz, C. Neely, and R. van der Hilst for providing additional comments on the manuscript, S. Johnson for help in producing Plate 3 and G. Laske for supplying the crustal model prior to publication. This research was supported by NSF grant EAR96-14350. M.P.F. is supported by a U.C. President's Postdoctoral Fellowship, NSF Postdoctoral Fellowship, and the Cecil H. and Ida M. Green Foundation.

References

Akaogi, M., and E. Ito, Refinement of enthalpy measurement of $MgSiO_3$ perovskite and negative pressure-temperature slopes for perovskite forming reactions, *Geophys. Res. Lett., 20*, 1839-1842, 1993.

Akaogi, M., A. Navrotsky, T. Yagi, and S. Akimoto, Pyroxene-garnet transformation: Thermochemistry and elasticity of garnet solid solutions, and application to a pyrolite mantle, in *High-Pressure Research in Mineral Physics, Geophys. Monogr. Ser.*, vol. 39, edited by M. H. Manghnani and Y. Syono, pp. 251-260, AGU, Washington, D.C., 1987.

Akaogi, M., E. Ito, and A. Navrotsky, Olivine-modified spinel-spinel transitions in the system Mg_2SiO_4-Fe_2SiO_4: Calorimetric measurements, thermochemical calculation, and geophysical application, *J. Geophys. Res., 94*, 15671-15685, 1989.

Anderson, D. L., and J. D. Bass, Transition region of the Earth's upper mantle, *Nature, 320*, 321-328, 1986.

Bijwaard, H., W. Spakman, and E. R. Engdahl, High resolution global delay time tomography, *EosTrans AGU, 77* (46), Fall Meet. Suppl., F482, 1996.

Bina, C. R., Mantle discontinuities, *U.S. Natl. Rep. Int. Union Geod. Geophys. 1987-1990, Rev. Geophys., 29*, 783-793, 1991.

Bina, C. R., and G. Helffrich, Phase transition Clapeyron slopes and transition zone seismic discontinuity topography, *J. Geophys. Res., 99*, 15,853-15,860, 1994.

Bina, C. R., and M. Kumazawa, Thermodynamic coupling of phase and chemical boundaries in planetary interiors, *Phys. Earth Planet. Inter.*, *76*, 329-341, 1993.

Bina, C. R., and B. J. Wood, The eclogite to garnetite transition--Experimental and thermodynamic constraints, *Geophys. Res. Lett.*, *11*, 955-958, 1984.

Bostock, M. G., *Ps* conversions from upper mantle transition zone beneath the Canadian landmass, *J. Geophys. Res.*, *101*, 8393-8402, 1996.

Brearley, A. J., D. C. Rubie, and E. Ito, Mechanisms of the transformations between the α, β, and γ polymorphs of Mg_2SiO_4 at 15 GPa, *Phys. Chem. Miner.*, *18*, 343-358, 1992.

Castle, J. C., and K. C. Creager, Imaging seismic velocity discontinuities of arbitrary orientation deep beneath Izu-Bonin, *Eos Trans. AGU*, *76* (46), Fall Meet. Suppl., F473, 1996.

Chopelas, A., Thermal properties of β-Mg_2SiO_4 at mantle pressures derived from vibrational spectroscopy: Implications for the mantle at 400 km depth, *J. Geophys. Res.*, *96*, 11,817-11829, 1991.

Christensen, U. R., and D. A. Yuen, The interaction of subducting lithospheric slab with a chemical or phase boundary, *J. Geophys. Res.*, *89*, 4389-4402, 1984.

Collier, J. D., and G. Helffrich, Topography of the "410" and "660" km seismic discontinuities in the Izu-Bonin subduction zone, *Geophys. Res. Lett.*, *24*, 1535-1538, 1997.

Creager, K. C., and T. H. Jordan, Slab penetration in the lower mantle beneath the Mariana and other island arcs of the northwest Pacific, *J. Geophys. Res.*, *91*, 3573-3589, 1986.

Ding, X. Y., and S. P. Grand, Seismic structure of the deep Kuril subduction zone, *J. Geophys. Res.*, *99*, 23,767-23,786, 1994.

Dueker, K. G., and A. F. Sheehan, Mantle discontinuity structure from midpoint stacks of converted *P* to *S* waves across the Yellowstone hotspot track, *J. Geophys. Res.*, *102*, 8313-8327, 1997.

Duffy, T. S., and D. L. Anderson, Seismic velocities in mantle minerals and the mineralogy of the upper mantle, *J. Geophys. Res.*, *94*, 1895-1912, 1989.

Dziewonski, A. M., and D. L. Anderson, Preliminary reference Earth model, *Phys. Earth Planet. Inter.*, *25*, 297-356, 1981.

Efron, B., and R. Tibshirani, Statistical data analysis in the computer age, *Science*, *253*, 390-395, 1991.

Engdahl, E. R., R. D. van der Hilst, and J. Berrocal, Imaging of subducted lithosphere beneath South America, *Geophys. Res. Lett.*, *22*, 2317-2320, 1995.

Flanagan, M. P. and P. M. Shearer, Topography on the 410-km seismic velocity discontinuity near subduction zones from stacking of *sS*, *sP*, and *pP* precursors, *J. Geophys. Res.*, in press, 1997.

Fukao, Y., M. Obayashi, and H. Inoue, Subducting slabs stagnant in the mantle transition zone, *J. Geophys. Res.*, *97*, 4809-4822, 1992.

Gossler, J., and R. Kind, Seismic evidence for very deep roots of continents, *Earth Planet. Sci. Lett.*, *138*, 1-13, 1996.

Grand, S. P., R. van der Hilst, and S. Widiyantoro, Global seismic tomography: A snapshot of convection in the Earth, *GSA Today*, *7*, 1-7, 1997.

Gu, Y., and A. M. Dziewonski, Global topography of upper mantle discontinuities from *SS* precursors, *Eos Trans. AGU*, *77* (46), Fall Meet. Suppl., F472, 1996.

Hager, B. H. and A. Raefsky, Deformation of seismic discontinuities and the state of mantle convection, *Eos Trans. AGU 62*, 1074, 1981.

Helffrich, G., and B. Wood, 410-km discontinuity sharpness and the form of the olivine α-β phase diagram: Resolution of apparent seismic contradictions, *Geophys. J. Int.*, *126*, F7-F12, 1996.

Honda, S., D. A. Yuen, S. Balachandar, and D. Reuteler, Three-dimensional instabilities of mantle convection with multiple phase transitions, *Science*, *259*, 1308-1311, 1993.

Ita, J., and L. Stixrude, Petrology, elasticity, and composition of the mantle transition zone, *J. Geophys. Res.*, *97*, 6849-6866, 1992.

Ito, E., and E. Takahashi, Postspinel transformations in the system Mg_2SiO_4-Fe_2SiO_4 and some geophysical implications, *J. Geophys. Res.*, *94*, 10,637-10,646, 1989.

Ito, E., and H. Yamada, Stability relations of silicate spinels, ilmenites and perovskites, in *High Pressure Research in Geophysics*, edited by S. Akimoto and M. Manghnani, pp. 405-419, Cent. for Acad. Pub.l, Tokyo, 1982.

Ito, E., M. Akaogi, L. Topor, and A. Navrotsky, Negative pressure-temperature slopes for reactions forming $MgSiO_3$ perovskite from calorimetry, *Science*, *249*, 1275-1278, 1990.

Jackson, I., Some geophysical constraints on the chemical composition of the Earth's lower mantle, *Earth Planet. Sci. Lett.*, *62*, 143-164, 1983.

Jeanloz, R., Effects of phase transitions and possible compositional changes on the seismological structure near 650 km depth, *Geophys. Res. Lett.*, *18*, 1743-1746, 1991.

Jordan, T. H., The continental tectosphere, *Rev. Geophys.*, *13*, 1-12, 1975.

Katsura, T., and E. Ito, The system Mg_2SiO_4-Fe_2SiO_4 at high pressures and temperatures: Precise determination of stabilities of olivine, modified spinel, and spinel, *J. Geophys. Res.*, *94*, 15,663-15,670, 1989.

Kennett, B. L. N., *IASPEI 1991 Seismological Tables*, 167 pp., Res. Sch. of Earth Sci., Aust. Natl. Univ., Canberra, Australia, 1991.

Lee, D.-K., and S. Grand, Depth of the upper mantle discontinuities beneath the East Pacific Rise, *Geophys. Res. Lett.*, *23*, 3369-3372, 1996.

Lerner-Lam, A. L., and T. H. Jordan, How thick are the continents?, *J. Geophys. Res.*, *92*, 14007-14026, 1987.

Li, A., K. Fischer, T. Clarke, M. Wysession, M. Fouch, and G. Al-Eqabi, Mantle discontinuities beneath eastern North America, *Eos Trans. AGU*, *77* (46), Fall Meet. Suppl., F474, 1996.

Machetel, P., and P. Weber, Intermittent layered convection in a model mantle with an endothermic phase change at 670 km, *Nature*, *350*, 55-57, 1991.

Masters, G., and H. Bolton, Large-scale shear velocity structure of the mantle, *Eos Trans. AGU*, *72* (44), Fall Meet. Suppl., 316, 1991.

Masters, G., S. Johnson, G. Laske, and H. Bolton, A shear-velocity model of the mantle, *Philos. Trans. R. Soc. London*, *354*, 1385-1411, 1996.

Mooney, W. D., G. Laske, and G. Masters, A new global crustal model at 5 x 5 degrees: CRUST5.0, *Eos Trans. AGU 76* (46), Fall Meet. Suppl., F421, 1995.

Neele, F., H. de Regt, and J. VanDecar, Gross errors in upper-mantle discontinuity topography from underside reflection data, *Geophys. J. Int.*, *129*, 194-204, 1997.

Niu, F., and H. Kawakatsu, Direct evidence for the undulation of the 660-km discontinuity beneath Tonga: Comparison of Japan and California array data, *Geophys. Res. Lett.*, *22*, 531-534, 1995.

Peltier, W. R., and L. P. Solheim, Mantle phase transitions and layered chaotic convection, *Geophys. Res. Lett.*, *19*, 321-324, 1992.

Petersen, N., J. Gossler, R. Kind, K. Stammler, and L. Vinnik, Precursors to *SS* and structure of the transition zone of the north-western Pacific, *Geophys. Res. Lett.*, *20*, 281-284, 1993.

Phipps Morgan, J., and P. M. Shearer, Seismic constraints on mantle flow and topography of the 660-km discontinuity: Evidence for whole mantle convection, *Nature*, *365*, 506-511, 1993.

Revenaugh, J. S., and T. H. Jordan, Mantle layering from *ScS* reverberations, 2, The transition zone, *J. Geophys. Res.*, *96*, 19763-19780, 1991.

Revenaugh, J. S., and S. A. Sipkin, Mantle discontinuity structure beneath China, *J. Geophys. Res.*, *99*, 21911-21927, 1994.

Richards, M. A., and C. W. Wicks, *S-P* conversion from the transition zone beneath Tonga and the nature of the 670 km discontinuity, *Geophys. J. Int.*, *101*, 1-35, 1990.

Rigden, S. M., G. D. Gwanmesia, J. D. F. Gerald, I. Jackson, and R. C. Liebermann, Spinel elasticity and seismic structure of the transition zone of the mantle, *Nature*, *354*, 143-145, 1991.

Ringwood, A. E., *Composition and Petrology of the Earth's Mantle*, 618 pp., McGraw-Hill, New York, 1975.

Ringwood, A. E., and T. Irifune, The nature of the 650-km discontinuity: Implications for mantle dynamics, *Nature*, *331*, 131-136, 1988.

Rubie, D. C., and A. J. Brearley, Phase transitions between β and γ $(Mg Fe)_2SiO_4$ in the Earth's mantle: Mechanisms and rheological implications, *Science*, *264*, 1445-1448, 1994.

Shearer, P. M., Constraints on upper mantle discontinuities from observations of long-period reflected and converted phases, *J. Geophys. Res.*, *96*, 18147-18182, 1991.

Shearer, P. M., Global mapping of upper mantle reflectors from long-period *SS* precursors, *Geophys. J. Int.*, *115*, 878-904, 1993.

Shearer, P. M., Transition zone velocity gradients and the 520-km discontinuity, *J. Geophys. Res.*, *101*, 3053-3066, 1996.

Shearer, P. M., and T. G. Masters, Global mapping of topography on the 660-km discontinuity, *Nature*, *355*, 791-795, 1992.

Shen, Y., S. C. Solomon, I. T. Bjarnason, and G. M. Purdy, Hot mantle transition zone beneath Iceland and the adjacent Mid-Atlantic Ridge

inferred from P-to-S conversions at the 410- and 660-km discontinuities, *Geophys. Res. Lett.., 23*, 3527-3530, 1996.

Silver, P. G., R. W. Carlson, and P. Olson, Deep slabs, geochemical heterogeneity, and the large-scale structure of mantle convection, *Annu. Rev. Earth Planet. Sci., 16*, 477-541, 1988.

Stammler, K., R. Kind, N. Petersen, G. Kosarev, L. Vinnik, and L. Qiyuan, The upper mantle discontinuities: Correlated or anticorrelated?, *Geophys. Res. Lett., 19*, 1563-1566, 1992.

Stixrude, L., Structure and sharpness of phase transitions mantle discontinuities, *J. Geophys. Res., 102*, 14835-14852, 1997.

Stixrude, L., R. J. Hemley, Y. Fei, and H. K. Mao, Thermoelasticity of silicate perovskite and magnesiowustite and stratification of the Earth's mantle, *Science, 257*, 1099-1101, 1992.

Su, W., R. L. Woodward, and A. M. Dziewonski, Degree 12 model of shear velocity heterogeneity in the mantle, *J. Geophys. Res., 99*, 6945-6980, 1994.

Tackley, P. J., D. J. Stevenson, G. A. Glatzmaier, and G. Schubert, Effects of an endothermic phase transition at 670 km depth in a spherical model of convection in the Earth's mantle, *Nature, 361*, 699-704, 1993.

van der Hilst, R., Complex morphology of subducted lithosphere in the mantle beneath the Tonga trench, *Nature, 374*, 154-157, 1995.

van der Hilst, R., R. Engdahl, W. Spakman, and G. Nolet, Tomographic imaging of subducted lithosphere below northwest Pacific island arcs, *Nature, 353*, 37-42, 1991.

van der Hilst, R., R. Engdahl, and W. Spakman, Tomographic inversion of P and pP data for aspherical mantle structure below northwest Pacific region, *Geophys. J. Int., 105*, 264-302, 1993.

van der Hilst, R., S. Widiyantoro, and E. R. Engdahl, Evidence for deep mantle circulation from global tomography, *Nature, 386*, 578-584, 1997.

Vasco, D. W., L. R. Johnson, and J. Pulliam, Lateral variations in mantle velocity structure and discontinuities determined from *P, PP, S, SS*, and *SS-SdS* travel time residuals, *J. Geophys. Res., 100*, 24037-24059, 1995.

Vidale, J. E., and H. M. Benz, Upper-mantle seismic discontinuities and the thermal structure of subduction zones, *Nature, 356*, 678-683, 1992.

Weber, M., and C. W. Wicks Jr., Reflections from a distant subduction zone, *Geophys. Res. Lett., 23*, 1453-1456, 1996.

Wicks, C. W., and M. A. Richards, A detailed map of the 660-kilometer discontinuity beneath the Izu-Bonin subduction zone, *Science, 261*, 1424-1427, 1993.

Widiyantoro, S., and R. van der Hilst, Structure and evolution of lithospheric slab beneath the Sunda Arc, Indonesia, *Science, 271*, 1566-1570, 1996.

Woodward, R. L., and G. Masters, Upper mantle structure from long-period differential travel times and free oscillation data, *Geophys. J. Int., 109*, 275-293, 1991.

Zhang, Z., and T. Lay, Investigation of upper mantle discontinuities near northwestern Pacific subduction zones using precursors to *sSH*, *J. Geophys. Res., 98*, 4389-4405, 1993.

M. P. Flanagan and P. M. Shearer, IGPP-0225, Scripps Institution of Oceanography, University of California at San Diego, 9500 Gilman Drive, La Jolla, CA 92093-0225. (email: megan@mahi.ucsd.edu; shearer@mahi.ucsd.edu)

(Received April 16, 1997; revised August 18, 1997;
accepted October 30, 1997.)